

# Cosmic homogeneity: the effect of redshift-space distortions and bias and cosmological constraints

Xiaoyun Shao,<sup>a,1</sup> Rodrigo Gonçalves,<sup>b,a</sup> Carlos A. P. Bengaly,<sup>a</sup>  
Gabriela C. Carvalho,<sup>c</sup> Jailson Alcaniz<sup>a</sup>

<sup>a</sup>Observatório Nacional, Rio de Janeiro - RJ, 20921-400, Brasil

<sup>b</sup>Departamento de Física, Universidade Federal Rural do Rio de Janeiro, Seropédica - RJ, 23897-000, Brasil

<sup>c</sup>Faculdade de Tecnologia, Universidade do Estado do Rio de Janeiro, 27537-000, Resende, RJ, Brazil

E-mail: [xiaoyun48@on.br](mailto:xiaoyun48@on.br); [rsousa@on.br](mailto:rsousa@on.br); [carlosbengaly@on.br](mailto:carlosbengaly@on.br);  
[gabriela.coutinho@fat.uerj.br](mailto:gabriela.coutinho@fat.uerj.br); [alcaniz@on.br](mailto:alcaniz@on.br)

**Abstract.** We present a novel cosmological analysis based on the angular correlation dimension  $D_2$  curve, a cumulative statistic derived from the two-point correlation function. Unlike traditional 3D approaches, angular  $D_2$  is inherently less sensitive to nonlinear dynamical distortions, such as the small-scale Finger-of-God (FoG) effect. Using both MultiDark-Patchy and EZmock galaxy catalogs, we assess the scale-dependent impact of redshift-space distortions on  $D_2$  and bias measurements. We demonstrate that the systematic errors associated with FoG modeling can be significantly reduced by restricting the analysis to appropriate minimum comoving angular scales of  $\sim 1.25^\circ$ , which corresponds to comoving scales of  $\sim 20 h^{-1}$  Mpc within the standard  $\Lambda$ CDM model. Since the observational estimative of  $D_2(\theta)$  is not dependent on a cosmological model we obtain robust estimates of the galaxy bias and place competitive constraints on the physical matter density  $\omega_m$ . By applying this framework to SDSS DR12 and DR16 Luminous Red Galaxy data, we obtain  $\omega_m = 0.142^{+0.014}_{-0.022}$  ( $1\sigma$ ), which agrees with current CMB analyses. Our results highlight the potential of the angular  $D_2$  curve as a model-independent and robust tool for cosmological parameter inference.

---

<sup>1</sup>Corresponding author

---

## Contents

<b>1</b>	<b>Introduction</b>	<b>1</b>
<b>2</b>	<b>Data</b>	<b>3</b>
2.1	Weights	5
<b>3</b>	<b>Correlation dimension and angular homogeneity scale</b>	<b>5</b>
3.1	Theoretical framework	5
3.2	Observational estimates of $D_2$ and $\theta_H$	6
<b>4</b>	<b>Theoretical impact of RSD on angular <math>D_2</math></b>	<b>8</b>
4.1	Redshift-Space Distortions	8
4.2	$D_2$ as a function of peculiar velocity dispersion	9
4.3	Theoretical comparison between linear and non-linear models	10
<b>5</b>	<b>Linear bias factor</b>	<b>11</b>
5.1	Theoretical analysis	11
5.2	The FoG effect on bias for mock catalogs	12
5.3	Bias measurement on DR12 and DR16 catalogs	15
<b>6</b>	<b>Cosmological constraints</b>	<b>17</b>
<b>7</b>	<b>Conclusions</b>	<b>19</b>

---

## 1 Introduction

The  $\Lambda$ -Cold Dark Matter ( $\Lambda$ CDM) framework forms the foundation of the Standard Cosmological Model (SCM), describing an expanding universe undergoing a late-time acceleration phase. Despite its success in explaining a wide range of cosmological observations - such as the Cosmic Microwave Background (CMB), the clustering and weak lensing of large-scale structures (LSS), and distances to standard candles like Type Ia Supernovae (SN) [1–6] - key components of the model, namely Cold Dark Matter (CDM) and dark energy ( $\Lambda$ ), remain mysterious.

The SCM faces significant theoretical and observational challenges. Theoretical issues include the coincidence and fine-tuning problems [7], while observationally, a roughly  $5\sigma$  tension exists between early and late-time measurements of the Hubble constant (see, e.g. [8] and references therein). Moreover, recent observations from the Dark Energy Spectroscopic Instrument (DESI) have hinted at the possibility of dynamic dark energy instead of a constant  $\Lambda$  [9], although this result remains debated [10, 11]. These challenges emphasize the importance of rigorously testing the fundamental assumptions of the SCM as any significant deviation would require a complete reformulation of the cosmological paradigm.

In view of these ongoing challenges, it becomes imperative to rigorously examine the foundational assumptions underlying the  $\Lambda$ CDM model. A central tenet of this framework is the Cosmological Principle (CP), which posits that the Universe is statistically homogeneous and isotropic on sufficiently large scales [12–15].

During the 1970s, Benoit Mandelbrot [16, 17] showed how the fractal or Hausdorff dimension (introduced in 1918 by mathematician Felix Hausdorff) is a rigorous way to characterize geometrical irregularities and chaos in Nature. The Hausdorff dimension estimate is independent of the amplitude of such irregularities and it only depends on how they scale with size. These ideas have been applied to galaxy surveys as a way to test if the metric of the Universe is geometrically homogeneous and isotropic [18–32], as well as to the CMB [33, 34].

An important way to investigate the CP is the analysis of the cosmic homogeneity through the fractal correlation dimension  $D_2$  [19], specifically taking into account the advantages of being intrinsically more sensitive to the shape of the large-scale structure clustering patterns than their amplitude. In the literature, there are two main approaches to the use of  $D_2$ . The first one is based on the spatial 3-dimensional separation  $r$  (so  $D_2 = D_2(r)$ ) of matter tracers, such as galaxies [24] and quasars [25, 28]. However, this analysis is model-dependent, since we need to assume a cosmological model to convert redshifts into distances, and thus it can only provide a consistency test of the CP assumption. The second one, is based on the angular 2-dimensional distribution of points  $\theta$  (so  $D_2 = D_2(\theta)$ ). Conversely from the former approach, this one can be carried out in a model independent way, because there is no conversion from redshift to distances. Note that this approach exhibits a reduced bin-to-bin correlations compared to the traditional two-point correlation function (2PCF) [29, 31, 32]. In both cases,  $D_2$  determine the scale on which the universe can be defined as homogeneous.

Moreover, it is worth mentioning that, in redshift space, the clustering of matter tracers exhibits distortions due to their peculiar velocities, which serves as a powerful probe for testing theories of gravity on large scales. This effect is called redshift-space distortion (RSD). There are two main aspects of those distortions, depending on the scale studied. On large scales, galaxies are falling into large gravitational potentials, which tend to sharpen their distribution along the line-of-sight in redshift space, a result that is known as Kaiser effect [35]. On small scales, the random velocity dispersion of galaxies along the line of sight leads to the so-called Finger-of-God (FoG) effect [36].

Early redshift space distortion measurements were primarily used to estimate the mean matter density,  $\Omega_m$ , which can be directly inferred from the growth rate  $f(z)$  under a given gravity model [37, 38]. Subsequently, it was demonstrated that RSDs can also be used effectively to discriminate between dark energy and modified gravity scenarios [39, 40]. As a result, RSD gained prominence as a key tool for probing gravity, leading to widespread applications across galaxy redshift surveys, both in the local Universe and at higher redshifts up to  $z \sim 1$ . Notable examples include 6dFGS [37], SDSS [38–40], WiggleZ [41, 42], VIPERS [43], and BOSS [44–46]. However, extracting unbiased cosmological constraints from RSD data requires precise modeling of the clustering signal, particularly at small scales where nonlinear dynamics become significant. This necessitates a careful characterization of the connection between observed tracers and the underlying dark matter distribution. However, discrepancies between observational measurements and the predictions of  $\Lambda$ CDM continue to persist, even when sophisticated RSD models are employed [47, 48].

Taking into account the advantages of the fractal dimension, we investigate how systematic errors that arises from redshift space distortion effects depend on the angular comoving scale. To achieve this, we first make use of realistic mock samples, specifically the MultiDark-Patchy mock catalogs [49, 50] and the EZmock galaxy catalogs [51], which are designed to replicate the SDSS DR12 and DR16 Luminous Red Galaxy (LRG) samples. We assess the systematic errors on the bias factor using these mock catalogs, and further extend the analysis to investigate systematic errors on the physical matter density ( $\omega_m$ ) using real data from

the SDSS DR12 and DR16 catalogs. We demonstrate that these systematic errors can be substantially reduced by restricting the fit to an appropriate range of comoving scales.

This paper is organized as follows: Sec. 2 describes the dataset applied. Sec. 3 presents the methodology, including the theoretical framework, redshift-space distortion modeling, and the estimation of the angular correlation dimension  $D_2(\theta)$ . In Sec. 4, we present the main results, focusing on the impact of the FoG effect on  $D_2$  and the bias parameter, both in mock catalogs and observational data from SDSS DR12 and DR16. Sec. 6 is dedicated to the cosmological analysis of  $\omega_m$ . We summarize our conclusions in Sec. 7.

## 2 Data

The Sloan Digital Sky Survey is a global scientific collaboration that has produced highly accurate three-dimensional maps of the Universe. The project was partitioned into four distinct phases: SDSS-I (2000-2005), SDSS-II (2005-2008), SDSS-III (2008-2014), and SDSS-IV (2014-2020). The present study focuses on the Data Release 12 (DR12) of the Baryon Oscillation Spectroscopic Survey<sup>1</sup> (BOSS) [52–54], and the Data Release 16 (DR16) of the extended Baryon Oscillation Spectroscopic Survey<sup>2</sup> (eBOSS) [55], which are subsets of the Sloan Digital Sky Survey III (SDSS-III) and Sloan Digital Sky Survey IV (SDSS-IV), respectively.

Specifically this work adopts the northern sky of both BOSS DR12 and eBOSS DR16 catalogues of Luminous Red Galaxies and for the sake of simplicity we hereafter name them as DR12 and DR16, respectively. The exclusion of the southern sky subsample is due to the limited sky coverage. The main features of the DR12 and DR16 data set used in this work are shown in Table 1 and Table 2, respectively. The redshift interval in each dataset is  $0.46 < z < 0.62$  with around 420,000 points (DR12) and  $0.67 < z < 0.74$  with approximately 30,000 points (DR16), as displayed in Fig.1. The footprint of the sky area coverage of both catalogues is shown in Fig.2.

We split the data into redshift bins of  $\Delta z = 0.01$ , with the size of the bin being chosen to avoid projection effects [56]. So we can avoid possible biases on homogeneity scale measure-

<sup>1</sup><https://live-sdss4org-dr12.pantheonsite.io/>

<sup>2</sup><https://www.sdss4.org/dr16/>

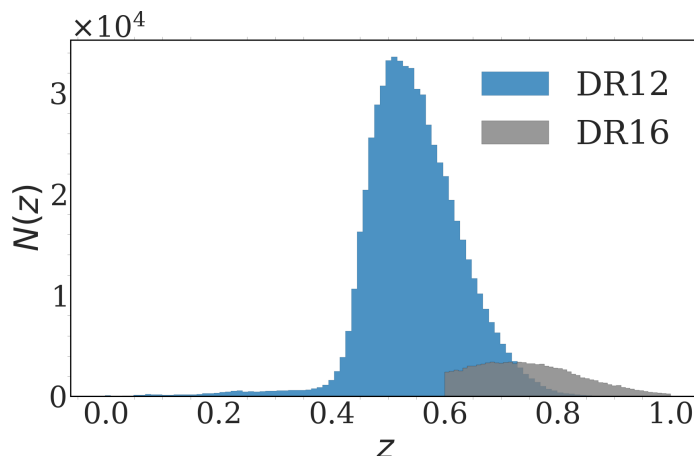


**Figure 1.** Redshift distributions of the LRGs from BOSS DR12 and eBOSS DR16 catalogues. We considered the redshift range  $0.46 < z < 0.74$ .

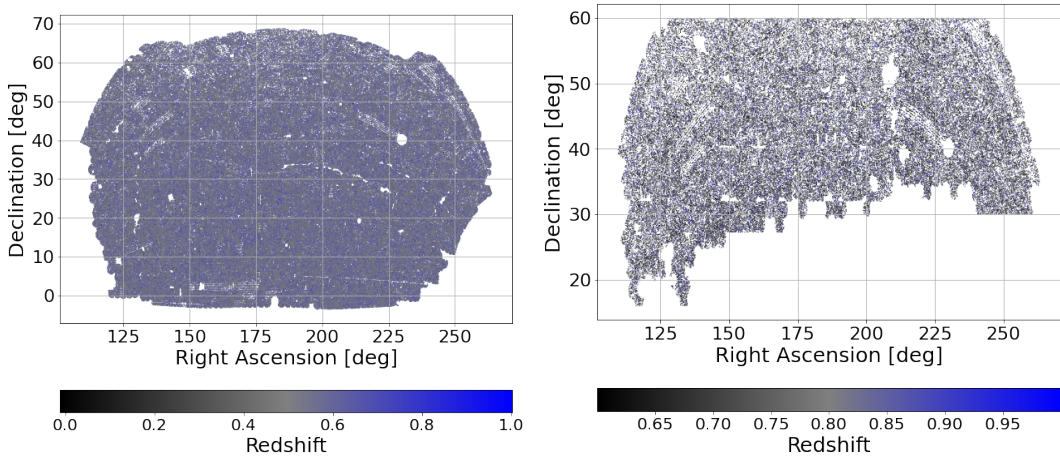


**Figure 2.** The footprint of DR12 and DR16, respectively

ments, and increase the number of data points, thus providing a good statistical performance for the analysis [57–60].

To test the robustness of the method and compute the covariance matrix, we rely on 1000 mock catalogs from the MultiDark-Patchy mock catalogs [49, 50] and the EZmock galaxy catalogues [51].

**Table 1.** The redshift bins adopted in our analysis from BOSS (DR12), along with the redshift bin means and corresponding number of LRGs in each bin.

$z$	$\bar{z}$	$N_{gal}$
0.46-0.47	0.465	22551
0.47-0.48	0.475	27319
0.48-0.49	0.485	29251
0.49-0.50	0.495	31763
0.50-0.51	0.505	33107
0.51-0.52	0.515	32887
0.52-0.53	0.525	32794
0.53-0.54	0.535	31995
0.54-0.55	0.545	31355
0.55-0.56	0.555	29486
0.56-0.57	0.565	28995
0.57-0.58	0.575	25289
0.58-0.59	0.585	23997
0.59-0.60	0.595	22568
0.60-0.61	0.605	20594
0.61-0.62	0.615	18799

**Table 2.** The redshift bins adopted in our analysis from eBOSS (DR16), along with the redshift bin means and corresponding number of LRGs in each bin.

$z$	$\bar{z}$	$N_{gal}$
0.67-0.68	0.675	4073
0.68-0.69	0.685	4222
0.69-0.70	0.695	4064
0.70-0.71	0.705	4209
0.71-0.72	0.715	4239
0.72-0.73	0.725	4084
0.73-0.74	0.735	4210

## 2.1 Weights

To correct for known clustering systematics, a specific weight is applied to each galaxy. For the DR12 samples, we followed the weighting scheme described in [61, 62], where the weight assigned to each galaxy is given by

$$w_{gal} = w_{FKP} * w_{sys} * (w_{cp} + w_{noz} - 1) \quad (2.1)$$

For the DR16 samples, we adopted the weighting described in [63–65]. Each galaxy is weighted as:

$$w_{tot} = w_{noz} w_{cp} w_{sys} w_{FKP} \quad (2.2)$$

where we use the FKP weight,  $w_{FKP}$ , [66] in order to reduce the variance of the two-point correlation function estimator.  $w_{systot} = w_{star} * w_{see}$  is the total angular systematic weight accounting for the seeing effect and the star confusion effect;  $w_{cp}$  accounts for the fact that the survey cannot spectroscopically observe two objects that are closer than  $62''$  [61, 62], and  $w_{noz}$  accounts for redshift failures.

## 3 Correlation dimension and angular homogeneity scale

### 3.1 Theoretical framework

In this section, we make an overview of the method that was developed to assess the correlation dimension ( $D_2$ ). For a complete description, we refer the reader to [31, 32], where this method is fully described.

The correlation dimension  $D_2$  is the key quantity for measuring the angular homogeneity scale of the data (see, e.g., [18, 31, 57–60, 62, 67–82] and references therein). In a few words the angular homogeneity scale ( $\theta_H$ ) is reached when  $D_2(\theta_H) = 1.98$ , by assuming an observational threshold of 1% [19].

As we are conducting a two-dimensional (2D) analysis, the correlation dimension is defined over the angular separation  $\theta$ . In this case the expression for the correlation dimension is given by

$$D_2(\theta) = 2 + \frac{d \ln}{d \ln \theta} \left[ 1 + \frac{1}{1 - \cos \theta} \int_0^\theta \omega(\theta') \sin \theta' d\theta' \right], \quad (3.1)$$

where  $\omega(\theta)$  is the 2D two-point angular correlation function (2PACF), which can be expressed as [83]

$$\omega(\theta) = \int dz_1 f(z_1) \int dz_2 f(z_2) \xi(r(z_1), r(z_2), \theta, \bar{z}) \quad (3.2)$$

where  $\xi$  is the 3D two-point correlation function for matter, as described below. Also, we assume  $f(z) \equiv b(z)\phi(z)$ , where  $\phi(z)$  denotes the radial selection, i.e., the probability to include a galaxy in a given redshift bin, and  $b(z)$  is the bias parameter, which relates the galaxy distribution to the underlying matter distribution.

In this paper, we consider only top-hat window functions and narrow redshift bins, so we compute the 2PACF and the 3D correlation function for matter as

$$\xi(r) = \frac{1}{2\pi^2} \int_0^\infty j_0(kr)k^2 P(k)dk, \quad (3.3)$$

where  $P(k)$  is the matter power spectrum and  $j_0(x) = \sin(x)/x$ . Also, the comoving distance to a certain redshift  $z$  is given by

$$r(z) = \int_0^z \frac{c}{H(z')} dz', \quad (3.4)$$

where

$$H(z) = H_0 \sqrt{\Omega_{m0}(1+z)^3 + (1-\Omega_{m0})}, \quad (3.5)$$

where  $H_0$  is the present-day Hubble parameter.

### 3.2 Observational estimates of $D_2$ and $\theta_H$

The above method describes how to obtain the theoretical predictions of  $D_2(\theta)$ . In what follows, we discuss how to estimate the relevant observational quantities. We assume the Landy-Szalay 2PACF estimator,  $\hat{\omega}_{ls}(\theta)$  [84], which is obtained directly from a combination of the data and random catalogues [59, 60, 79]. It is defined as

$$\hat{\omega}_{ls}(\theta) = \frac{DD(\theta) - 2DR(\theta) + RR(\theta)}{RR(\theta)}, \quad (3.6)$$

where  $DD(\theta)$ ,  $DR(\theta)$ , and  $RR(\theta)$  are the numbers of pairs of data as a function of their separations  $\theta$ , normalized by the total number of pairs, in data-data, data-random and random-random catalogues, respectively. The pair-counting was done with the TREECORR package [85]. Concerning to the random catalogues, we use the BOSS and eBOSS catalogues, which are approximately 50 and 20 times larger than the respective real catalogues [52–55]. This ensures that the statistical fluctuations caused by the random points are insignificant.

Therefore, in order to calculate the  $D_2$  values and uncertainties, we perform the following steps: (i) we calculate the value of  $D_2$  using Eqs. 3.1 and 3.6 for different values of  $\theta$ ; (ii) we repeat this procedure 1000 times via bootstrap resampling technique; (iii) we calculate the mean and standard deviation of the values obtained in step (ii) as our measurements of the  $D_2$  and its corresponding uncertainty.

We perform this analysis by using the observational samples mentioned in the previous section (SDSS DR12 and DR16, Tables 1 and 2, respectively) for each redshift bin. Table 3 presents the angular homogeneity scales  $\theta_H$  across all redshift bins, including results from both bootstrap resampling and mock catalogs. This table allows a direct comparison between the observational and simulated estimates of the homogeneity scale, and provides insight into the consistency and redshift evolution of large-scale structure homogeneity. For the sake of example, we present the result for the bin  $0.55 < z < 0.56$ . Fig. 3 presents the observed angular correlation function  $\omega(\theta)$  (left) and the angular correlation dimension  $D_2(\theta)$  (right) as a function of angular separation  $\theta$  (in degrees) in the redshift bin  $z \in [0.55, 0.56]$ . Black

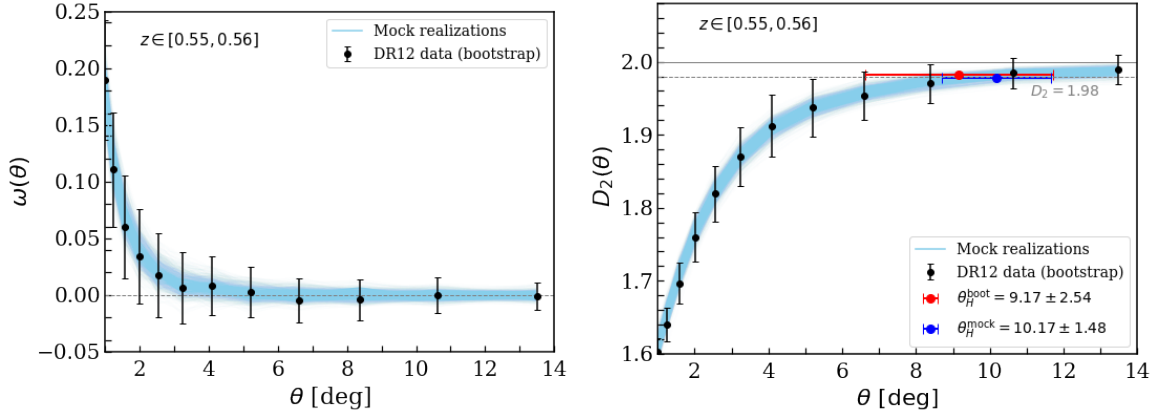


**Figure 3.** Observed angular correlation function(left) and angular correlation dimension  $D_2(\theta)$  (right) for DR12 in the Redshift Bin  $z \in [0.55, 0.56]$

$\bar{z}$	$\theta_H^{\text{boot}}$ [deg]	$\theta_H^{\text{mock}}$ [deg]
0.465	$10.4 \pm 2.47$	$12.07 \pm 1.46$
0.475	$10.43 \pm 2.58$	$11.70 \pm 1.53$
0.485	$9.70 \pm 2.73$	$11.44 \pm 1.53$
0.495	$9.08 \pm 2.50$	$11.30 \pm 1.55$
0.505	$9.14 \pm 2.48$	$11.18 \pm 1.57$
0.515	$9.28 \pm 2.76$	$10.97 \pm 1.55$
0.525	$9.57 \pm 2.39$	$10.71 \pm 1.56$
0.535	$9.80 \pm 2.67$	$10.63 \pm 1.49$
0.545	$9.72 \pm 2.69$	$10.36 \pm 1.54$
0.555	$9.17 \pm 2.54$	$10.17 \pm 1.48$
0.565	$9.35 \pm 2.77$	$10.20 \pm 1.51$
0.575	$9.07 \pm 2.75$	$10.08 \pm 1.47$
0.585	$8.31 \pm 2.63$	$9.78 \pm 1.43$
0.595	$8.88 \pm 2.87$	$9.63 \pm 1.38$
0.605	$8.54 \pm 2.90$	$9.49 \pm 1.35$
0.615	$8.36 \pm 2.90$	$9.32 \pm 1.24$
0.675	$7.49 \pm 2.83$	$8.53 \pm 1.73$
0.685	$8.53 \pm 2.58$	$8.51 \pm 1.84$
0.695	$8.07 \pm 2.59$	$8.41 \pm 1.74$
0.705	$7.36 \pm 2.49$	$8.09 \pm 1.70$
0.715	$6.92 \pm 2.28$	$7.93 \pm 1.70$
0.725	$8.12 \pm 2.04$	$8.01 \pm 1.74$
0.735	$8.89 \pm 2.90$	$7.87 \pm 1.66$

**Table 3.** Angular homogeneity scales  $\theta_H$  obtained from both bootstrap resampling and mock catalogs, across all redshift bins.

points show the measured values from the data, with error bars estimated via 1000 bootstrap resampling. Light blue curves correspond to 1000 mock catalogs, illustrating the expected range of  $D_2(\theta)$  under  $\Lambda$ CDM model. The horizontal dashed line at  $D_2(\theta) = 1.98$  defines the homogeneity threshold. Red and blue error bars indicate the homogeneity scale  $\theta_H$ , defined as

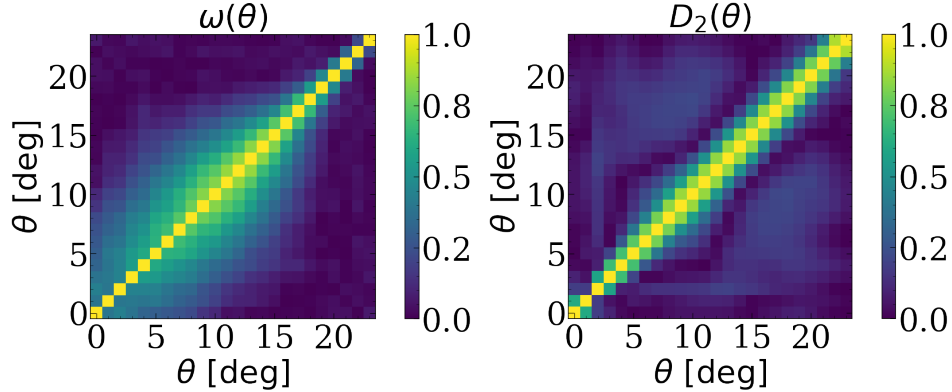


**Figure 4.** Absolute Correlation Matrices  $|\rho_{ij}|$  of  $\omega(\theta)$  and  $D_2(\theta)$  from 1000 Mock Realizations in the Redshift Bin  $z \in [0.55, 0.56]$

the scale at which  $D_2(\theta)$  approaches 1.98, estimated from bootstrap (red) and mocks (blue), respectively,  $\theta_H^{\text{boot}} = 9.17 \pm 2.54^\circ$ , and  $\theta_H^{\text{mock}} = 10.75 \pm 1.53^\circ$ . The comparison shows that both data and mocks reach homogeneity on mean scales around  $9^\circ$ - $10^\circ$ , at the redshift mean  $\bar{z} = 0.555$ , consistent with  $\Lambda$ CDM expectations.

Fig. 4 shows the absolute Pearson correlation matrices  $|\rho_{ij}|$  computed from 1000 mock realizations of the angular correlation function  $\omega(\theta)$  (left) and the angular correlation dimension  $D_2(\theta)$  (right). Each pixel represents the strength of the correlation between two angular bins  $\theta_i$  and  $\theta_j$ , with  $|\rho_{ij}| = 1$  (yellow) indicating perfect correlation and  $|\rho_{ij}| = 0$  (dark purple) indicating no linear correlation. The  $D_2(\theta)$  matrix exhibits significantly reduced off-diagonal correlations compared to  $\omega(\theta)$ , indicating lower bin-to-bin covariance. This highlights the advantage of  $D_2(\theta)$  as a decorrelated and robust summary statistic for angular clustering analysis.

## 4 Theoretical impact of RSD on angular $D_2$

### 4.1 Redshift-Space Distortions

A deeper study on the two-point correlation function should take into account non-linear effects on the matter power spectrum. The theoretical prediction of the non-linear  $P(k)$  is commonly computed by using only CAMB [86] in combination with HALOFIT corrections [87]. However, it is necessary to model the impact of redshift-space distortions on these theoretical predictions.

With effect, in real space, the matter power spectrum, denoted by  $P_{\delta\delta}^{(r)}(k)$ , describes the clustering of the underlying dark matter density field. To model the galaxy power spectrum in redshift space,  $P_{gg}^{(s)}(k)$ , two main effects must be taken into account. On large scales, the Kaiser effect leads to a modification on the power spectrum given by

$$P_{gg}^{(s)}(k, \mu; b) = b^2 (1 + \beta\mu^2)^2 P_{\delta\delta}^{(r)}(k), \quad (4.1)$$

where  $b$  is the linear bias factor,  $\beta = f/b$ , and  $f$  is the linear growth rate, approximated as  $f \simeq \Omega_m^{0.55}(z)$  [88]. On small scales, the distortion originated from the Finger-of-God is a non-linear effect that can be modeled using a Gaussian damping function that depends on the pairwise velocity dispersion  $\sigma_p$  [36]:

$$\ln D(k, \mu; \sigma_p) = -\frac{1}{2} \left( \frac{k\sigma_p\mu}{H_0} \right)^2. \quad (4.2)$$

Combining both effects, the full galaxy power spectrum in redshift space is expressed as:

$$P_{gg}^{(s)}(k; b, \sigma_p) = b^2 \int_0^1 (1 + \beta\mu^2)^2 D(k, \mu; \sigma_p) d\mu P_{\delta\delta}^{(r)}(k). \quad (4.3)$$

By applying a Fast Fourier Transform (FFT) to  $P_{gg}^{(s)}(k)$ , we obtain the 3D two-point correlation function in redshift space:

$$\xi^{(s)}(r; b, \sigma_p) = \text{FFT} \left[ P_{gg}^{(s)}(k; b, \sigma_p) \right]. \quad (4.4)$$

The redshift-space distortion (RSD) plays a crucial role in the calculation of the power spectrum  $P(k)$  and, consequently, the correlation dimension  $D_2(\theta)$  (Eqs. 3.1 and 3.2). On large scales, the Kaiser effect can be accurately modeled using Eq. 4.1, while on small scales, the Finger-of-God (FoG) effect is typically modeled by Eq. 4.2. However, the theoretical model for RSD (Eq. 4.2) is not perfectly accurate at small scales due to the inherently nonlinear behavior of gravity in these regimes. One direct way to reduce the resulting systematic errors would be to improve the modeling of RSD at nonlinear scales (see, e.g., [43, 89–92]), but in this work, we adopt a different strategy, as described below.

## 4.2 $D_2$ as a function of peculiar velocity dispersion

In the present paper we investigate how the systematic errors depend on the choice of angular separation considered in the analysis. Specifically, we assess the accuracy of the theoretical model without the FoG effect as a function of  $\theta$ . We verify that selecting an appropriate minimum angular scale for the fit of the whole  $D_2(\theta)$  curve allows the impact of the FoG effect to be minimized, thereby making the contribution of nonlinear effects negligible. It is worth to note that in all analyses we are still taking into account the Kaiser effect. A key advantage of this approach is that it requires only a minimal number of free parameters for the modeling, simplifying the analysis while maintaining robustness.

For the sake of illustration Figure 5 shows the theoretical angular correlation dimension  $D_2(\theta)$  as a function of angular separation  $\theta$  (in degrees) at redshift  $z = 0.555$ , accounting for the effects of line-of-sight velocity dispersion from 0 to 600 km/s. Each curve corresponds to a different value of  $\sigma_p$ , with  $\sigma_p = 0$  at the bottom and increasing upward to  $\sigma_p = 600$  km/s. Larger peculiar velocity dispersions increase the correlation dimension  $D_2(\theta)$  at small angular scales, driving it closer to the homogeneous value of 2. The horizontal dashed line marks the homogeneity threshold  $D_2 = 1.98$ . The inset panel zooms in on small angular separations  $\theta \in [0, 2^\circ]$ .

According to [62], pairwise peculiar-velocity dispersion  $\sigma_p$  for SDSS luminosity galaxies is around 250 km/s. The range of velocity dispersion from 0 to 600 km/s is reasonable and well includes the velocity dispersion of SDSS luminosity galaxies. This analysis shows that peculiar velocities have a significant scale-dependent impact on  $D_2(\theta)$  on small-degree angular separations. However, for angular scales greater than  $\theta = 1.25$  degree (vertical dashed line), the effect of peculiar velocity dispersions on  $D_2(\theta)$  decreases significantly. We also carried out the same test in different redshift bins, and we found that the same conclusion is valid.

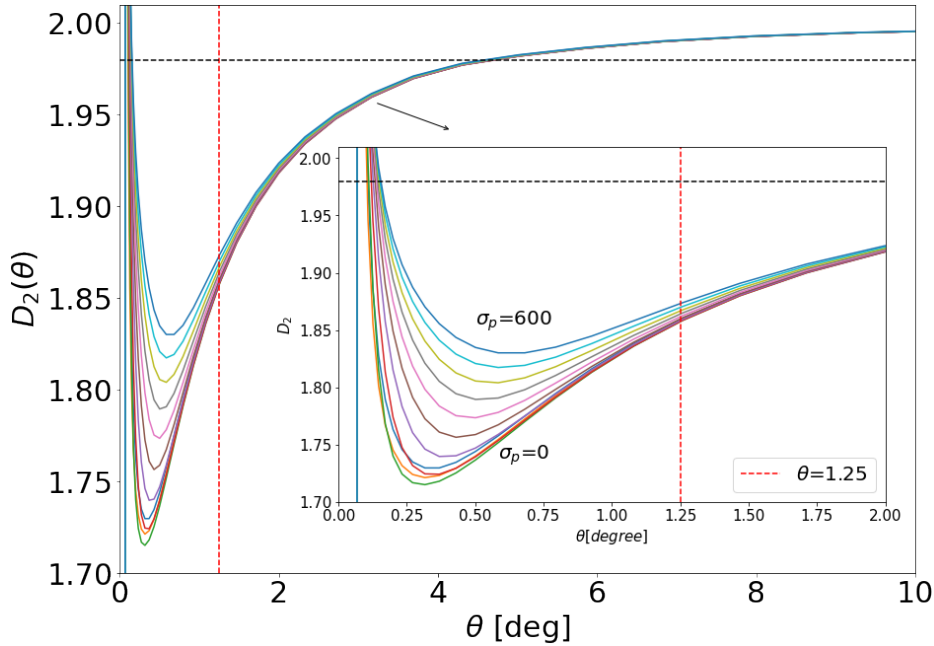


**Figure 5.** Theoretical angular Correlation Dimension  $D_2(\theta)$  at  $z = 0.555$  for peculiar-velocity dispersion  $\sigma_p \in [0, 600]$  km/s.

### 4.3 Theoretical comparison between linear and non-linear models

To address the impact of the Finger-of-God (FOG) effect, we compare two scenarios: one including the effect (NL model, Eq. 4.3) and one excluding it (LIN model, Eq. 4.1). As shown in Fig. 6, the black open circles represent the full set of mock data points generated using the NL model (Eq. 4.3) with a fixed bias ( $b = 1$ ) and a velocity dispersion of  $\sigma_p = 600$  km/s. From this set, we select subsets beginning at different minimum angular scales,  $\theta_{\min}$ <sup>3</sup>, to be used as data for fitting. We perform fits using the LIN model (Eq. 4.1) over two ranges:  $\theta \geq 0.5^\circ$  (so  $\theta_{\min} = 0.5^\circ$ ) and  $\theta \geq 1.25^\circ$  (so  $\theta_{\min} = 1.25^\circ$ ). In these fits, the bias is treated as a free parameter, while all other cosmological parameters are held fixed to the Planck 2018 best-fit values. The resulting best-fit curves are shown as dashed blue and red lines for the two respective angular cuts.

The bottom panel of Fig. 6 shows the percentage deviations between the LIN model predictions and the NL model-generated points, with blue squares and red circles (as in the top panel) indicating the residuals corresponding to the two angular fitting ranges. The LIN model fitted over  $\theta_{\min} = 0.5^\circ$  (dashed blue curve) exhibits larger deviations compared to the fit over  $\theta_{\min} = 1.25^\circ$  (dashed red curve). This result demonstrates that increasing the minimum angular scale  $\theta_{\min}$  improves the consistency between the NL model-generated data and the LIN model predictions, which do not account for the FoG effect.

<sup>3</sup>When we refer to a minimum angle we are implicitly describing an analysis through a whole range of angles, where  $\theta_{\min}$  represents the initial value.

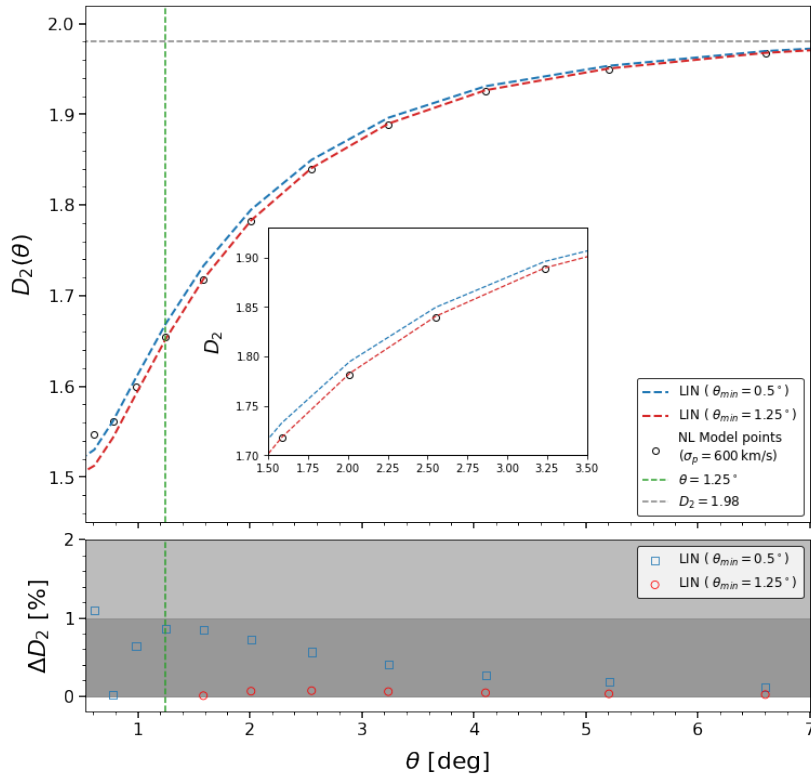


**Figure 6.** Top panel: Best-fit values of  $D_2(\theta)$  for data points generated from the NL model by applying Eq. 4.3 with  $\sigma_p = 600$  km/s (black open circles). The dashed blue and red curves represent fits to these model-generated points using the LIN model defined in Eq. 4.1, performed over angular ranges  $\theta > 0.5^\circ$  and  $\theta > 1.25^\circ$ , respectively. The horizontal dashed gray line marks the reference homogeneity scale  $D_2 = 1.98$ , while the vertical dashed green line indicates  $\theta = 1.25^\circ$ . The inset highlights small angular scales ( $1.5^\circ \lesssim \theta \lesssim 3.5^\circ$ ), emphasizing differences between NL model-generated points and LIN model predictions. Bottom panel: Percentage deviations between the LIN model predictions and NL model-generated values. The blue squares and red circles (as in the top panel) represent the residuals for the two angular fitting ranges. Shaded gray bands indicate thresholds of  $\pm 1\%$  and  $\pm 2\%$ , illustrating the level of agreement between the LIN and NL models across different angular scales. The vertical dashed green line again marks  $\theta = 1.25^\circ$ .

## 5 Linear bias factor

### 5.1 Theoretical analysis

After that, we proceed to study the Finger-of-God impact on bias. Firstly, we perform a statistical analysis in which we use the generated data presented in the previous section (with the NL model and  $\sigma_p = 600$  km/s) and fit the bias assuming it as a free parameter. Then we compare the best-fit value with the fixed bias originally assumed,  $b = 1$ . In Fig. 7, we present the relative difference between the recovered best-fit bias and the reference bias, as a function of the minimum angular scale  $\theta_{min}$ , at redshift  $z = 0.555$ . The red points show the best-fit results at different  $\theta_{min}$  values. The vertical dashed lines correspond to  $\theta = 1.25^\circ$  (green),  $\theta = 1.5^\circ$  (red), and  $\theta = 2.0^\circ$  (blue).

When  $\theta_{min}$  exceeds 1.25 degrees, the relative uncertainty remains below 0.5%, indicating excellent agreement. As  $\theta_{min}$  increases, the bias estimation becomes more stable and less

sensitive to residual Finger-of-God effects, as expected, since we are moving far away from the non-linear regime peculiar to the small angle scales. However, when  $\theta_{min}$  surpasses 4 degrees, the relative uncertainty increases due to the reduced number of available data points from the whole curve. After that we move our analysis to mock and real data catalogue, as follows.

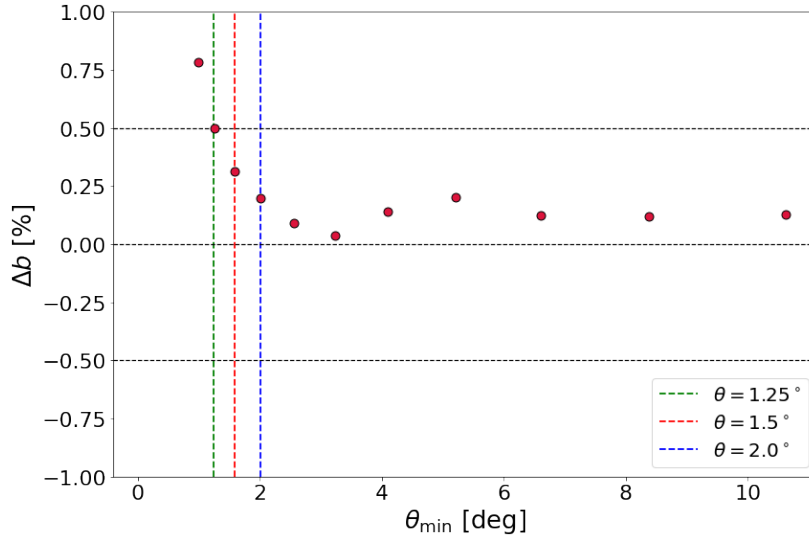


**Figure 7.** The relative difference between the recovered best-fit bias and the reference bias at redshift  $z = 0.555$ , expressed as  $100 \cdot \frac{b - b_{ref}}{b_{ref}}$ . The red points represent the best-fit results obtained at various  $\theta_{min}$  values, while the vertical dashed lines mark  $\theta = 1.25^\circ$  (green),  $\theta = 1.5^\circ$  (red), and  $\theta = 2.0^\circ$  (blue).

## 5.2 The FoG effect on bias for mock catalogs

The most direct way to investigate systematic errors from the non-linear FoG model is to use large numerical simulations and apply to them the same analysis techniques employed for real data. So we begin by inferring  $D_2(\theta)$  using the MultiDark-Patchy mock catalogs and fitting the results with both the linear Kaiser model (Eq. 4.1, LIN) and the nonlinear Finger-of-God model (Eq. 4.3, NL).

The top panel of Fig. 8 displays the best-fit values of  $D_2(\theta)$  as a function of angular separation  $\theta$ . The dashed and solid curves correspond to fits based on the linear (LIN) and nonlinear (NL) models, respectively. The bottom panel presents the percentage systematic errors, defined as  $(100 \cdot (D_2^{model} - D_2^{mock})/D_2^{mock})$ , quantifying the relative difference between theoretical predictions and mock measurements.

For  $\theta_{min} = 0.5^\circ$ , with the nonlinear (NL) model (blue solid), we obtain a bias of  $b = 1.914 \pm 0.038$  and a pairwise velocity dispersion of  $\sigma_p = 263 \pm 40$  km/s, with a reduced  $\chi^2 = 0.90$ , while, with the linear (LIN) model, we find  $b = 1.902 \pm 0.030$  and a reduced  $\chi^2 = 0.93$  (blue dashed). These results are consistent with the bias values reported in [62], where  $b = 1.944 \pm 0.021$  and  $\sigma_p = 252 \pm 8.9$  km/s, with a reduced  $\chi^2 = 0.91$ . The velocity dispersion we find is also in agreement with the typical value for CMASS galaxy samples,  $\sigma_p = 240 \pm 50$  km/s [93].

As illustrated in the top panel of Fig. 8, when fitting the mock catalog measurements starting from 0.5 degree ( $\theta_{min} = 0.5^\circ$ ), both the linear Kaiser model (LIN, blue dashed) and

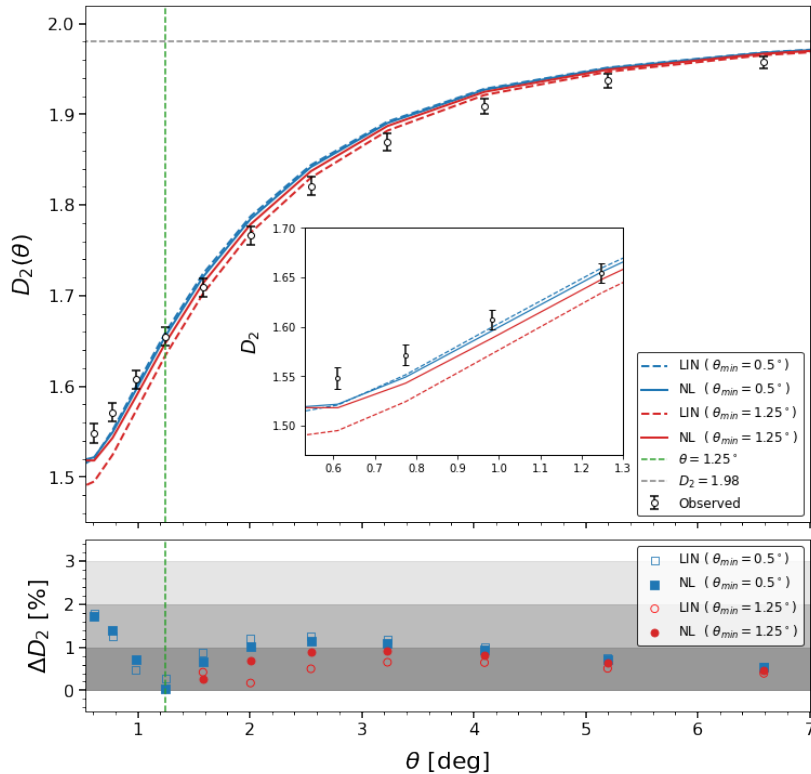


**Figure 8.** Top panel: Best-fit values of  $D_2(\theta)$  for mock catalogs at  $z = 0.555$ . The dashed and solid blue curves show the results obtained by fitting the mock data with the models defined in Eq. 4.1 and Eq. 4.3, respectively, over the scale range ( $\theta > 0.5^\circ$ ), whereas the dashed and solid red curves correspond to fits using the same models, respectively, but applied over the range ( $\theta > 1.25^\circ$ ). Black data points with  $1\text{-}\sigma$  error bars represent the mock measurements mean values and standard deviations, respectively. The horizontal dashed gray line indicates the homogeneity scale reference value ( $D_2 = 1.98$ ), and the vertical dashed green line marks ( $\theta = 1.25^\circ$ ). An inset zooms in on small angular scales from  $0.5^\circ$  to  $1.3^\circ$ , clearly illustrating the differences between mock measurements and model predictions in that regime. Bottom panel: percentage systematic errors on ( $D_2(\theta)$ ), defined as  $100(D_2^{model} - D_2^{mock})/D_2^{mock}$ , i.e., the percentage differences between theoretical predictions and observational data. Symbols indicate residuals for LIN and NL models, with the same color coding as above. The shaded gray bands represent deviations of  $\pm 1\%$ ,  $\pm 2\%$ , and  $\pm 3\%$ , illustrating how closely models match observations across different angular scales. Again, the vertical green dashed line again marks the angle ( $\theta = 1.25^\circ$ ).

the nonlinear dispersion model (NL, blue solid) provide an good description of  $D_2(\theta)$  at angular scales  $\theta > 1.25^\circ$ . However, significant deviations emerge at smaller angular separations ( $\theta < 1.25^\circ$ ), where neither model is able to accurately capture the characteristic suppression induced by nonlinear FoG effects. This is anticipated for the LIN model (blue dashed), which neglects nonlinear velocity dispersion. In the case of the NL model (blue solid), the residual discrepancies are attributed to the limitations of the dispersion model in accurately modeling nonlinear redshift-space distortions, as highlighted in the inset of Fig. 8. While the NL model based on Eq.4.3 partially mitigates the deviations in  $D_2$ , it fails to fully reconcile the model predictions with the mock measurements — a result consistent with earlier studies (e.g., [48, 94] and references therein).

As shown in the bottom panel of Fig. 8, the best-fit values of  $D_2(\theta)$  exhibit systematic deviations from the mock measurements, with the magnitude of the bias varying as a function of angular scale  $\theta$ . For fits performed over the full angular range starting from 0.5 degree ( $\theta_{min} = 0.5^\circ$ ), both the linear model (open blue squares) and the nonlinear dispersion model (solid blue squares) yield percentage differences of approximately 2% at small scales. When the fitting is performed over the full range starting from 1.25 degree ( $\theta_{min} = 1.25^\circ$ ), the discrepancies are noticeably reduced to approximately 1% for both the LIN (open red squares) and NL (solid red squares) cases. Indeed, limiting the full fitting range to start from 1.25 degree ( $\theta_{min} = 1.25^\circ$ ) hardly affects the results: we obtain  $b = 1.951 \pm 0.039$  for the NL model and  $b = 1.950 \pm 0.037$  for the LIN model. These values are in excellent agreement with those obtained using  $\theta_{min} = 0.5^\circ$ , indicating that our bias estimation is quite robust. Furthermore, the derived bias values are consistent with those reported by several other authors [36, 95–99].

This result indicates that the angular ranges adopted are sufficiently large to limit the systematic errors on  $(D_2(\theta))$ . In particular, by selecting a minimum angular scale of ( $\theta_{min} = 1.25^\circ$ ), one can significantly mitigate systematic biases in  $(D_2(\theta))$  without requiring a more sophisticated modeling of nonlinear effects. Notably, discrepancies between observational measurements and  $\Lambda$ CDM predictions persist, even when employing a range of nonlinear redshift-space distortion (RSD) models – many of which are more accurate than the dispersion model adopted in this work [47, 48] – which suggests that residual modeling uncertainties may still be present, even in these more advanced RSD frameworks. In this context, excluding the small-scale regime where nonlinearities become significant appears to be a more effective strategy than attempting to model these effects using the empirical approach of Eq. 4.3.

We then procedure to apply only the linear Kaiser model (Eq. 4.1) to estimate the bias parameter using the MultiDark-Patchy mock catalogs (so do not take into account the nonlinear FoG effect). The relative difference between the recovered best-fit bias and the reference bias as a function of the minimum angular scale  $\theta_{min}$  is shown in Fig. 9. In this analysis, the reference bias ( $b_{ref}$ ) is taken from Table 2 of [62], where the FoG effect was included in their bias estimation.

As shown in Fig. 9, the relative uncertainty of bias exceeds 5% when  $\theta_{min}$  is below 1.25 degrees, where the deviation from the reference bias is larger due to residual FoG effects. However, when  $\theta_{min}$  lies within the range of 1.25 to 3 degrees, the relative uncertainty remains consistently below 5%. For values of  $\theta_{min}$  greater than 4 degrees, the relative uncertainty rises again, primarily due to fewer data points available for analysis. Despite this increase in uncertainty compared with Fig. 7, this trend aligns well with the theoretical expectations.

Our analysis indicates that the bias parameter can be reliably recovered when  $\theta_{min}$  lies in the range of  $1.25^\circ$  to  $3^\circ$ , corresponding to comoving distances of approximately 20–48  $h^{-1}$  Mpc. Furthermore, the reduced chi-squared values— $\chi^2_\nu = 0.93$  for  $\theta_{min} = 1.25^\circ$  and  $\chi^2_\nu = 0.96$  for  $\theta_{min} = 1.5^\circ$ —demonstrate that the model without the FoG effect provides a good fit to the data within this range. This conclusion remains valid across other redshift bins.

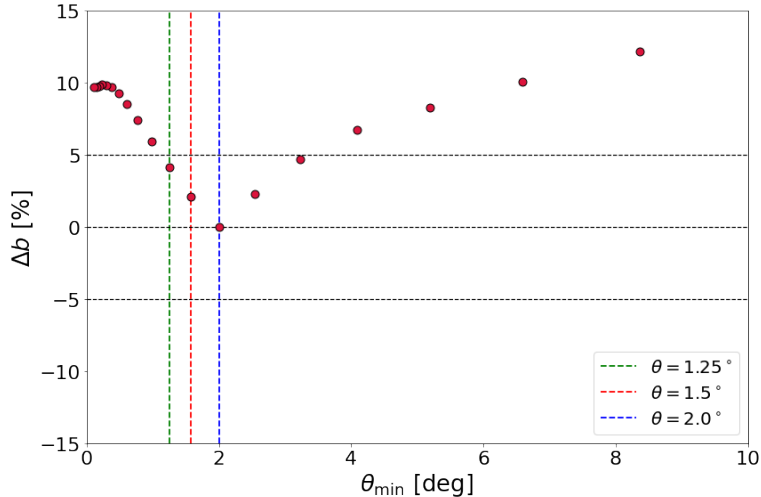


**Figure 9.** Relative deviation between the recovered best-fit galaxy bias and the reference bias for the mock catalogs at redshift  $z = 0.555$ , expressed as  $\Delta b = 100 \cdot \frac{b - b_{\text{ref}}}{b_{\text{ref}}}$ . The red points represent the best-fit results obtained for different values of  $\theta_{\text{min}}$ , while the vertical dashed lines indicate  $\theta_{\text{min}} = 1.25^\circ$  (green),  $\theta_{\text{min}} = 1.5^\circ$  (red), and  $\theta_{\text{min}} = 2.0^\circ$  (blue).

### 5.3 Bias measurement on DR12 and DR16 catalogs

As established in the previous section, the optimal range for  $\theta_{\text{min}}$  lies between  $1.25^\circ$  and  $3^\circ$ , within which our LIN model — even neglecting the FoG effect — can reliably recover the galaxy bias parameter. Based on this finding, we now perform measurements using real data from the SDSS DR12 and DR16 catalogs, adopting a lower bound of  $\theta_{\text{min}} = 1.25^\circ$ .

In Fig. 10, we show the correlation dimension  $D_2(\theta)$  as a function of angular separation  $\theta$  at representative redshift  $z = 0.555$ . The blue points represent all measured data, while

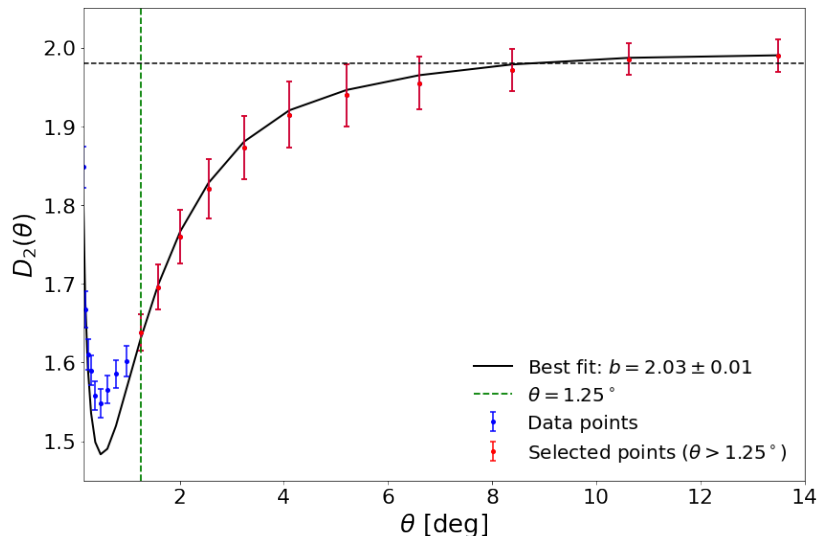


**Figure 10.** The correlation dimension  $D_2(\theta)$  as a function of angular separation  $\theta$  at redshift mean  $\bar{z} = 0.555$  for the real observational data

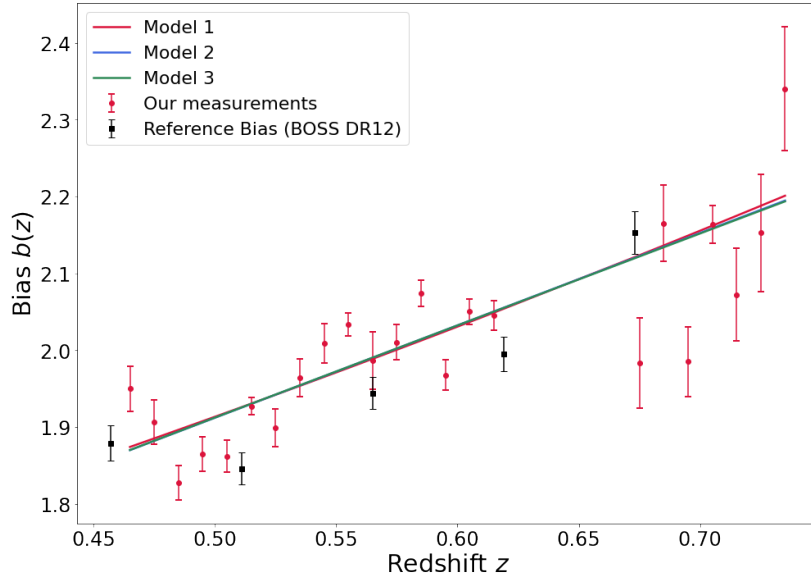


**Figure 11.** The measured galaxy bias from the DR12 and DR16 catalogs is shown. The red points represent our measurements, with error bars indicating statistical uncertainties, while the black points correspond to the reference bias values reported in [62]. The three colored lines represent different bias evolution models: Model 1 (red line), Model 2 (blue line), and Model 3 (green line).

the red points indicate the selected subset used for fitting, starting from a minimum angular scale of  $\theta_{min} = 1.25^\circ$  (marked by the green dashed line). The black curve shows the best-fit theoretical model, yielding a bias parameter of  $b = 2.03 \pm 0.01$ . Error bars represent the statistical uncertainties in each bin.

We also conduct the bias measurements across the 23 redshift bins spanning the range  $0.46 \leq z \leq 0.74$  and presented in Section 3.2. The full results are shown in Fig. 11, where the measured galaxy bias is shown as a function of redshift using real data. The red points with error bars represent our bias measurements, while black points with error bars denote the reference values from Table 2 of [62], which are based on the SDSS DR12 analysis, which accounts for the FoG effect.

The figure illustrates the redshift evolution of the galaxy bias parameter  $b(z)$ , along with three theoretical fitting models:

- Model 1:  $b(z) = a_1 + a_2(1 + z)^2$
- Model 2:  $b(z) = a_1 + a_2(1 + z)$
- Model 3:  $b(z) = a_1 \frac{1+z}{(1+z_{\text{eff}})^{a_2}}$ , where  $z_{\text{eff}}$  denotes the effective redshift of the bin (as in [100], [101]).

In Table 4 we present the best fit values of the parameters for each model. The corresponding reduced chi-squared values for these fits are 4.57, 4.48, and 4.47, respectively for each model. The third model (shown in green) provides the best fit, though the improvement over the others is not significant.

Our measurements (red points) show good agreement with the reference values (black points), particularly at intermediate redshifts. At higher redshifts, the scatter and uncertainties increase, due to reduced data density and larger observational errors. As demonstrated

Model	$a_1$	$a_2$	$\chi_\nu^2$
Model 1	$1.061 \pm 0.131$	$0.379 \pm 0.054$	4.57
Model 2	$0.106 \pm 0.263$	$1.204 \pm 0.169$	4.48
Model 3	$2.020 \pm 0.011$	$0.944 \pm 0.131$	4.47

**Table 4.** Best-fit values of  $a_1$  and  $a_2$  for the different bias models, along with the corresponding reduced  $\chi^2$  assuming 21 degrees of freedom.

above, it is indeed possible to achieve nearly unbiased constraints on the bias factor from  $D_2$  across all redshifts considered for the DR12 and DR16 samples. A key advantage of this method is the minimal number of free parameters required for the modeling.

## 6 Cosmological constraints

Differently from the analysis of Sec. 5.3, here we jointly constrain the bias factor,  $b$ , and the physical matter density,  $\omega_m$ . Additionally, in this section we investigate the accuracy of the constraints on  $\omega_m$  provided by our theoretical model without FoG effect, as a function of angular scale. From the observational point of view we use the SDSS DR12 and DR16 datasets described in Sec. 2. We then perform a Markov Chain Monte Carlo (MCMC) analysis, based on measurements of the correlation dimension  $D_2$ . The analysis is made within the framework of a spatially flat  $\Lambda$ CDM model, explicitly  $\omega_m$  is a free parameter,  $b$  is modeled using Bias Model 3 (Section 5.3) and we marginalize over the nuisance bias parameters  $a_1$  and  $a_2$ . We have also tested alternative bias models and found that they do not significantly affect our results. The remaining fiducial cosmological parameters,  $p_F = (n_s, \ln[10^{10} A_s], \Omega_k)$ , are fixed to their best-fit values from the Planck 2018 results [1]. The chi-squared function used in this analysis is defined as:

$$\chi^2 = \sum_{ij} \left[ D_2 - D_2^{\text{th}}(b, \omega_m, p_F) \right] C_{ij}^{-1} \left[ D_2 - D_2^{\text{th}}(b, \omega_m, p_F) \right] \quad (6.1)$$

where  $D_2$  denotes the observed correlation dimension, and  $C_{ij}$  is the covariance matrix derived from the MultiDark-Patchy mock catalogs [49, 50] and the EZmock galaxy catalogues [51]. The theoretical prediction  $D_2^{\text{th}}$  represents the model correlation dimension of the galaxy distribution correspondent to the theoretical curve obtained from the parameters previously described.

Figure 12 shows the constraints on the physical matter density  $\omega_m$  and its comparison with the CMB value as a function of the minimum angular scale  $\theta_{min}$  used in the analysis. The top panel shows that the best-fit  $\omega_m$  values obtained from MCMC fits to the correlation dimension  $D_2$ , with red points and error bars representing the measurements and their uncertainties. The dashed lines indicate the Planck 2018 CMB constraint on  $\omega_m$ . The bottom panel shows the corresponding tension in units of standard deviation  $\sigma$  relative to the CMB constraint. Shaded regions mark the  $0.5\sigma$ ,  $1\sigma$ , and  $2\sigma$  confidence levels. For the sake of example, for  $\theta_{min} = 1.25^\circ$  we obtain a constraint of  $\omega_m(\theta_{min} = 1.25^\circ) = 0.142_{-0.022}^{+0.014}$  from our data, which is in excellent agreement with the Planck CMB result,  $\omega_m = 0.1434 \pm 0.0020$ , with a discrepancy of only  $0.2\sigma$ .

As we can also see in Figure 12, for low  $\theta_{min}$  values (e.g., below 1 degree), the tension exceeds  $1.5\sigma$  and even approaches  $2\sigma$ , indicating that the  $\omega_m$  inferred from  $D_2$  differs from the CMB value. This significant discrepancy is mainly caused by non-linear FoG effect,

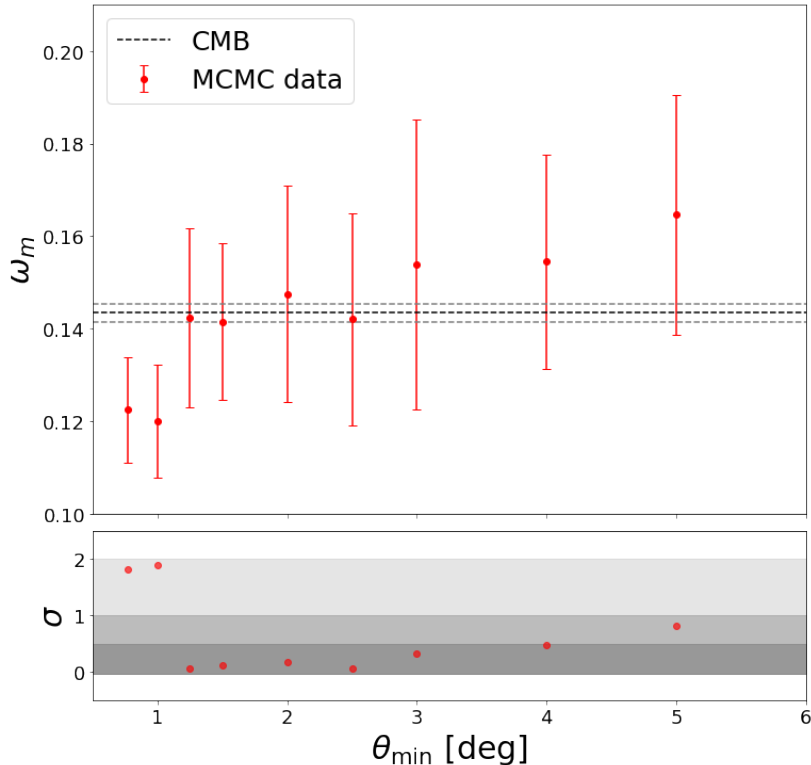


**Figure 12.** Constraints on  $\omega_m$  and its comparison with CMB at  $1\sigma$  confidence level as a function of  $\theta_{min}$ . The shaded horizontal bands correspond to  $0.5\sigma$  (dark gray),  $1\sigma$  (gray), and  $2\sigma$  (light gray) intervals.

which distorts clustering measurements at small scales due to random peculiar velocities in collapsed structures. As  $\theta_{min}$  increases to values between 1.25 degree and 3 degree, the tension drops below  $1\sigma$  and even below  $0.5\sigma$ , leading to much better consistency between the two measurements. For  $\theta_{min} > 4$  degree, the tension slightly increases again, which is due to the smaller number of available data points.

These results suggest that angular scales in the range  $\theta_{min} \sim 1.25^\circ - 3^\circ$  are optimal for minimizing tension and avoiding nonlinear distortions, making them ideal for robust cosmological parameter estimation from  $D_2$ .

Based on that we assume  $\theta_{min} = 1.25^\circ$  and we constrain the cosmological parameters  $\Omega_{m0}$  and  $H_0$ , via MCMC analysis, as shown in Fig. 13. The prior on  $\Omega_{m0}$  is taken to be uniform in the range  $[0.05, 1.0]$ , and the prior on  $H_0$  is uniform in the range  $[20, 100]$ .

We found the best fit of the Hubble constant as  $H_0 = 74.9^{+5.8}_{-7.9}$  km.s $^{-1}$ .Mpc $^{-1}$ , which agrees with the best-fit from both SN and Planck CMB observations. It is worth mentioning that given the bigger uncertainty in our estimate compared to Planck CMB and SN, one cannot definitively conclude whether it favors early-time measurements or late-time measurements.

We also found the best fit of the matter density parameter as  $\Omega_{m0} = 0.254 \pm 0.023$ . This is in good agreement with the independent analysis of [102], which used gas mass fraction measurements in galaxy clusters and obtained  $\Omega_{m0} = 0.285 \pm 0.013$ , corresponding to a discrepancy of only  $0.65\sigma$ . Our best-fit value of  $\Omega_{m0}$  is also in agreement with the result of [103], within  $0.67\sigma$ , where they reported  $\Omega_{m0} = 0.286^{+0.011}_{-0.013}$ . Their analysis is based on

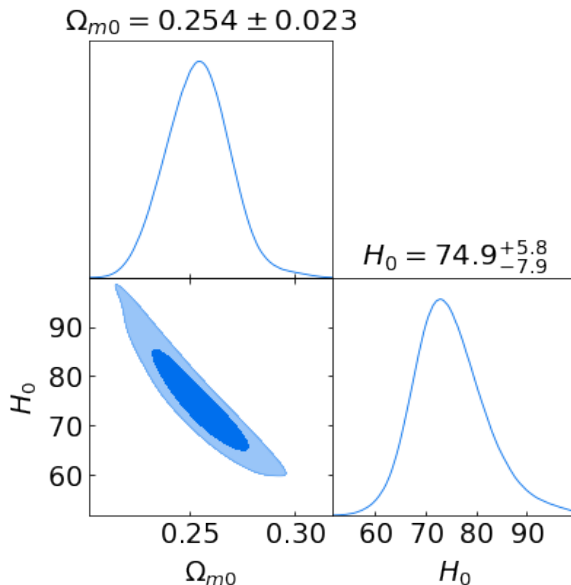


**Figure 13.** Posterior distributions of  $\Omega_{m0}$  and  $H_0$  from the  $D_2(\theta)$  analysis performed with MCMC.

the average of the two-point correlation function (2PCF) using combined data from BOSS, eBOSS, and DES, and includes information from the range ( $20 h^{-1} \text{ Mpc} < s < 160 h^{-1} \text{ Mpc}$ ). For our analysis, we restrict the minimum angular separation to  $\theta_{min} = 1.25^\circ$ , corresponding to comoving scales of approximately  $20 h^{-1} \text{ Mpc}$ , with the fiducial model used. We note that our best-fit value of  $\Omega_{m0}$  is slightly smaller (but still consistent within  $1\sigma$ ) compared to the value derived from BAO datasets, which combine measurements from the SDSS DR7 main galaxy sample [104], the 6dF Galaxy Survey [37], and the SDSS BOSS DR12 [105] and eBOSS DR16 surveys [106], without assuming priors on the sound horizon scale at the drag epoch  $r_{drag}$ , yielding  $\Omega_{m0} = 0.293^{+0.13}_{-0.15}$ . Nonetheless, this difference is not unexpected, given the distinct methodologies employed.

## 7 Conclusions

In this work, we addressed the challenge posed by the inaccurate modeling of non-linear motions at small scales within the dispersion model, which can lead to biased constraints on the galaxy bias factor and the physical matter density  $\omega_m$ . Rather than attempting to refine the model to better capture small-scale nonlinearities, we demonstrate that nearly unbiased constraints on the bias factor and cosmological parameters can be obtained by modeling the angular correlation dimension function  $D_2(\theta)$ . This approach is valid since the analysis is restricted to sufficiently large scales where non-linear effects are negligible, then neglecting the necessity of robustly modeling the uncertainties and improving redshift-space distortions (RSD) at small scales.

The angular correlation dimension  $D_2(\theta)$  is a cumulative statistic derived from the two-point correlation function and serves as a powerful and model-independent probe of cosmic homogeneity. Initially we found the cosmic homogeneity scale  $\theta_H$  values for 23 bins across the redshift range  $0.46 < z < 0.74$ , based on the observational SDSS DR12 and DR16 Luminous Red Galaxy (LRG) catalogs. We then comprehensively explored the full angular interval of

the  $D_2$  curve, so differently from the general literature of cosmic homogeneity that basically focus on the  $\theta_H$ . We developed such a study by varying the starting angles  $\theta_{min}$ , then we systematically defined and investigated the impact of  $\theta_{min}$  on our analyses and estimates of cosmological parameters.

The next step was to investigate the redshift-space distortion effects, namely the Kaiser effect (a linear modeling that depends on the bias factor) and the non-linear Finger-of-God (FoG) effect (dependent on the velocity dispersion). We performed a theoretical analysis demonstrating how the theoretical  $D_2$  curves change based on the peculiar velocity assumed in the non-linear model. To validate our methodology, we employed realistic mock catalogs (MultiDark-Patchy and EZmock galaxy catalogs), assuming a fiducial bias ( $b = 1$ ) and a velocity dispersion ( $\sigma_P = 600$  km/s) to generate  $D_2$  values. We then fitted these mock data using only the linear model within a  $\Lambda$ CDM fiducial model, with bias as the only free parameter, testing various  $\theta_{min}$  values. This analysis revealed how  $\theta_{min}$  impacts the fitted bias, consistently pointing to  $\theta_{min} \approx 1.25^\circ$  as the optimal choice. This angle value corresponds to a comoving distances of  $\sim 20 h^{-1}$ Mpc and allows the use of the simpler linear model and avoid to characterize a non-linear model, which demands a precise understanding of the assumed velocity dispersion.

Based once more on the LRG catalogs from SDSS DR12 and DR16 we calculated the linear bias factor for the same 23 redshift bins previously mentioned. We obtained bias values typically between 1.8 and 2.3, consistent with a redshift evolution. We then fitted three different theoretical parameterizations to the observed bias evolution in redshift, finding no significant discrepancies between them.

Finally, we imposed constraints on cosmological parameters using our observational data, in the context of  $\Lambda$ CDM paradigm. We initially investigated the physical matter density parameter ( $\omega_m$ ) with varying  $\theta_{min}$  values. The lowest  $\theta_{min}$  that produced results consistent with Planck CMB was found to be  $1.25^\circ$ . So, based on the previous analysis, we fixed  $\theta_{min} = 1.25^\circ$ , then we restricted the matter density parameter ( $\Omega_m$ ) and the Hubble constant ( $H_0$ ), marginalizing over the other parameters. Our best fit yielded  $\Omega_{m0} = 0.254 \pm 0.023$  and  $H_0 = 74.9^{+5.8}_{-7.9}$  at  $1\sigma$  level. Our results demonstrate that the angular correlation dimension curve provides a powerful and complementary probe of cosmology, offering unbiased constraints on cosmological parameters by judiciously handling redshift-space distortions at small scales.

## Acknowledgments

XS is supported by Fundação de Amparo à Pesquisa do Estado do Rio de Janeiro (FAPERJ). RSG thanks financial support from FAPERJ grant No. 260003/005977/2024 - APQ1. JSA is supported by CNPq grant No. 307683/2022-2 and FAPERJ grant No. 259610 (2021). This work was developed thanks to the use of the National Observatory Data Center (CPDON).

## References

- [1] N Aghanim, Y Akrami, M Ashdown, J Aumont, C Baccigalupi, M Ballardini, AJ Banday, RB Barreiro, N Bartolo, S Basak, et al. Planck 2018 results-vi. cosmological parameters (corrigendum). *Astronomy & Astrophysics*, 652:C4, 2021.
- [2] Dillon Brout et al. The Pantheon+ Analysis: Cosmological Constraints. *Astrophys. J.*, 938(2):110, 2022.

- [3] Shadab Alam et al. Completed SDSS-IV extended Baryon Oscillation Spectroscopic Survey: Cosmological implications from two decades of spectroscopic surveys at the Apache Point Observatory. *Phys. Rev. D*, 103(8):083533, 2021.
- [4] T. M. C. Abbott et al. Dark Energy Survey Year 3 results: Cosmological constraints from galaxy clustering and weak lensing. *Phys. Rev. D*, 105(2):023520, 2022.
- [5] Mathew S. Madhavacheril et al. The Atacama Cosmology Telescope: DR6 Gravitational Lensing Map and Cosmological Parameters. *Astrophys. J.*, 962(2):113, 2024.
- [6] Xiangchong Li et al. Hyper Suprime-Cam Year 3 results: Cosmology from cosmic shear two-point correlation functions. *Phys. Rev. D*, 108(12):123518, 2023.
- [7] Steven Weinberg. The Cosmological constant problems. 5 2000.
- [8] Eleonora Di Valentino, Olga Mena, Supriya Pan, Luca Visinelli, Weiqiang Yang, Alessandro Melchiorri, David F. Mota, Adam G. Riess, and Joseph Silk. In the realm of the Hubble tension—a review of solutions. *Class. Quant. Grav.*, 38(15):153001, 2021.
- [9] A. G. Adame et al. DESI 2024 VI: Cosmological Constraints from the Measurements of Baryon Acoustic Oscillations. 4 2024.
- [10] R. Calderon et al. DESI 2024: Reconstructing Dark Energy using Crossing Statistics with DESI DR1 BAO data. 5 2024.
- [11] Marina Cortês and Andrew R. Liddle. Interpreting DESI’s evidence for evolving dark energy. 4 2024.
- [12] Chris Clarkson and Roy Maartens. Inhomogeneity and the foundations of concordance cosmology. *Classical and Quantum Gravity*, 27(12):124008, 2010.
- [13] Roy Maartens. Is the Universe homogeneous? *Phil. Trans. Roy. Soc. Lond. A*, 369:5115–5137, 2011.
- [14] Chris Clarkson. Establishing homogeneity of the universe in the shadow of dark energy. *Comptes Rendus Physique*, 13:682–718, 2012.
- [15] Pavan Kumar Aluri, Paolo Cea, Pravabati Chingambam, Ming-Chung Chu, Roger G Clowes, Damien Hutsemékers, Joby P Kochappan, Alexia M Lopez, Lang Liu, Niels C M Martens, C J A P Martins, Konstantinos Migkas, Eoin Ó Colgáin, Pratyush Pranav, Lior Shamir, Ashok K Singal, M M Sheikh-Jabbari, Jenny Wagner, Shao-Jiang Wang, David L Wiltshire, Shek Yeung, Lu Yin, and Wen Zhao. Is the observable universe consistent with the cosmological principle? *Classical and Quantum Gravity*, 40(9):094001, April 2023.
- [16] Benoit B Mandelbrot. The fractal geometry of nature wh freeman and co. *New York*, 1982.
- [17] BB Mandelbrot. Galaxy distributions and fractals. *Astrophysical Letters and Communications*, Vol. 36, Nos. 1-6, p. 1-5, 36:1–5, 1997.
- [18] David W. Hogg, Daniel J. Eisenstein, Michael R. Blanton, Neta A. Bahcall, J. Brinkmann, James E. Gunn, and Donald P. Schneider. Cosmic homogeneity demonstrated with luminous red galaxies. *Astrophys. J.*, 624:54–58, 2005.
- [19] Morag I Scrimgeour, Tamara Davis, Chris Blake, J Berian James, Gregory B Poole, Lister Staveley-Smith, Sarah Brough, Matthew Colless, Carlos Contreras, Warrick Couch, et al. The wigglez dark energy survey: the transition to large-scale cosmic homogeneity. *Monthly Notices of the Royal Astronomical Society*, 425(1):116–134, 2012.
- [20] D. Alonso, A. Bueno Belloso, F. J. Sánchez, J. Garcia-Bellido, and E. Sánchez. Measuring the transition to homogeneity with photometric redshift surveys. *MNRAS*, 440(1):10–23, May 2014.
- [21] David Alonso, Ana Isabel Salvador, Francisco Javier Sánchez, Maciej Bilicki, Juan García-Bellido, and Eusebio Sánchez. Homogeneity and isotropy in the two micron all sky

survey photometric redshift catalogue. *Monthly Notices of the Royal Astronomical Society*, 449(1):670–684, 2015.

- [22] Pierre Laurent, Jean-Marc Le Goff, Etienne Burtin, Jean-Christophe Hamilton, David W Hogg, Adam Myers, Pierros Ntelis, Isabelle Pâris, James Rich, Eric Aubourg, et al. A 14 h- 3 gpc<sup>3</sup> study of cosmic homogeneity using boss dr12 quasar sample. *Journal of Cosmology and Astroparticle Physics*, 2016(11):060, 2016.
- [23] Pierros Ntelis, Jean-Christophe Hamilton, Jean-Marc Le Goff, Etienne Burtin, Pierre Laurent, James Rich, Jeremy Tinker, Eric Aubourg, Héliion Du Mas Des Bourboux, Julian Bautista, et al. Exploring cosmic homogeneity with the boss dr12 galaxy sample. *Journal of Cosmology and Astroparticle Physics*, 2017(06):019, 2017.
- [24] RS Gonçalves, GC Carvalho, CAP Bengaly Jr, JC Carvalho, A Bernui, JS Alcaniz, and R Maartens. Cosmic homogeneity: a spectroscopic and model-independent measurement. *Monthly Notices of the Royal Astronomical Society: Letters*, 475(1):L20–L24, 2018.
- [25] RS Gonçalves, GC Carvalho, CAP Bengaly, JC Carvalho, and JS Alcaniz. Measuring the scale of cosmic homogeneity with sdss-iv dr14 quasars. *Monthly Notices of the Royal Astronomical Society*, 481(4):5270–5274, 2018.
- [26] Nathan J. Secrest, Sebastian von Hausegger, Mohamed Rameez, Roya Mohayaee, Subir Sarkar, and Jacques Colin. A Test of the Cosmological Principle with Quasars. *ApJL*, 908(2):L51, 2021.
- [27] Carlos AP Bengaly, Roy Maartens, and Mario G Santos. Probing the cosmological principle in the counts of radio galaxies at different frequencies. *Journal of Cosmology and Astroparticle Physics*, 2018(04):031, 2018.
- [28] Rodrigo S Gonçalves, Gabriela C Carvalho, Uendert Andrade, Carlos AP Bengaly, Joel C Carvalho, and Jailson Alcaniz. Measuring the cosmic homogeneity scale with sdss-iv dr16 quasars. *Journal of Cosmology and Astroparticle Physics*, 2021(03):029, 2021.
- [29] Uendert Andrade, Rodrigo S Gonçalves, Gabriela C Carvalho, Carlos AP Bengaly, Joel C Carvalho, and Jailson Alcaniz. The angular scale of homogeneity with sdss-iv dr16 luminous red galaxies. *Journal of Cosmology and Astroparticle Physics*, 2022(10):088, 2022.
- [30] Vasudev Mittal, Oliver T Oayda, and Geraint F Lewis. The cosmic dipole in the quiaia sample of quasars: a bayesian analysis. *Monthly Notices of the Royal Astronomical Society*, 527(3):8497–8510, 2024.
- [31] Xiaoyun Shao, Rodrigo S. Gonçalves, Carlos A. P. Bengaly, Uendert Andrade, Gabriela C. Carvalho, and Jailson Alcaniz. Can the angular scale of cosmic homogeneity be used as a cosmological test? *Eur. Phys. J. C*, 84(7):655, 2024.
- [32] Xiaoyun Shao, Carlos A. P. Bengaly, Rodrigo S. Gonçalves, Gabriela C. Carvalho, and Jailson Alcaniz. Cosmological constraints from angular homogeneity scale measurements. *Eur. Phys. J. C*, 85(3):225, 2025.
- [33] Benjamin Camacho-Quevedo and Enrique Gaztañaga. A measurement of the scale of homogeneity in the early universe. *Journal of Cosmology and Astroparticle Physics*, 2022(04):044, 2022.
- [34] Xiaoyun Shao, Facundo Toscano, Diego Garcia Lambas, Rodrigo S. Gonçalves, Carlos A. P. Bengaly, Heliana E. Luparello, Frode K. Hansen, and Jailson Alcaniz. Revisiting the CMB homogeneity scale: low multipoles removal effect and extragalactic foreground masking. 5 2025.
- [35] Nick Kaiser. Clustering in real space and in redshift space. *Monthly Notices of the Royal Astronomical Society*, 227(1):1–21, 1987.

- [36] WE Ballinger, JA Peacock, and AF Heavens. Measuring the cosmological constant with redshift surveys. *Monthly Notices of the Royal Astronomical Society*, 282(3):877–888, 1996.
- [37] Florian Beutler, Chris Blake, Matthew Colless, D Heath Jones, Lister Staveley-Smith, Lachlan Campbell, Quentin Parker, Will Saunders, and Fred Watson. The 6df galaxy survey: baryon acoustic oscillations and the local hubble constant. *Monthly Notices of the Royal Astronomical Society*, 416(4):3017–3032, 2011.
- [38] Lado Samushia, Will J Percival, and Alvise Raccanelli. Interpreting large-scale redshift-space distortion measurements. *Monthly Notices of the Royal Astronomical Society*, 420(3):2102–2119, 2012.
- [39] Chia-Hsun Chuang and Yun Wang. Modelling the anisotropic two-point galaxy correlation function on small scales and single-probe measurements of  $h(z)$ ,  $d_a(z)$  and  $f(z) \sigma_8(z)$  from the sloan digital sky survey dr7 luminous red galaxies. *Monthly Notices of the Royal Astronomical Society*, 435(1):255–262, 2013.
- [40] Chia-Hsun Chuang, Francisco Prada, Antonio J Cuesta, Daniel J Eisenstein, Eyal Kazin, Nikhil Padmanabhan, Ariel G Sánchez, Xiaoying Xu, Florian Beutler, Marc Manera, et al. The clustering of galaxies in the sdss-iii baryon oscillation spectroscopic survey: single-probe measurements and the strong power of  $f(z) \sigma_8(z)$  on constraining dark energy. *Monthly Notices of the Royal Astronomical Society*, 433(4):3559–3571, 2013.
- [41] Chris Blake, Sarah Brough, Matthew Colless, Carlos Contreras, Warrick Couch, Scott Croom, Darren Croton, Tamara M Davis, Michael J Drinkwater, Karl Forster, et al. The wigglez dark energy survey: Joint measurements of the expansion and growth history at  $z < 1$ . *Monthly Notices of the Royal Astronomical Society*, 425(1):405–414, 2012.
- [42] Carlos Contreras, Chris Blake, Gregory B Poole, Felipe Marin, Sarah Brough, Matthew Colless, Warrick Couch, Scott Croom, Darren Croton, Tamara M Davis, et al. The wigglez dark energy survey: measuring the cosmic growth rate with the two-point galaxy correlation function. *Monthly Notices of the Royal Astronomical Society*, 430(2):924–933, 2013.
- [43] S de la Torre, L Guzzo, JA Peacock, E Branchini, A Iovino, BR Granett, U Abbas, C Adami, S Arnouts, J Bel, et al. The vimos public extragalactic redshift survey (vipers): galaxy clustering and redshift-space distortions at  $z \simeq 0.8$  in the first data release. 2013.
- [44] Rita Tojeiro, Will J Percival, Jon Brinkmann, Joel R Brownstein, Daniel J Eisenstein, Marc Manera, Claudia Maraston, Cameron K McBride, Demitri Muna, Beth Reid, et al. The clustering of galaxies in the sdss-iii baryon oscillation spectroscopic survey: measuring structure growth using passive galaxies. *Monthly Notices of the Royal Astronomical Society*, 424(3):2339–2344, 2012.
- [45] Beth A Reid, Lado Samushia, Martin White, Will J Percival, Marc Manera, Nikhil Padmanabhan, Ashley J Ross, Ariel G Sánchez, Stephen Bailey, Dmitry Bizyaev, et al. The clustering of galaxies in the sdss-iii baryon oscillation spectroscopic survey: measurements of the growth of structure and expansion rate at  $z = 0.57$  from anisotropic clustering. *Monthly Notices of the Royal Astronomical Society*, 426(4):2719–2737, 2012.
- [46] Beth A Reid, Hee-Jong Seo, Alexie Leauthaud, Jeremy L Tinker, and Martin White. A 2.5 per cent measurement of the growth rate from small-scale redshift space clustering of sdss-iii cmass galaxies. *Monthly Notices of the Royal Astronomical Society*, 444(1):476–502, 2014.
- [47] Edward Macaulay, Ingunn Kathrine Wehus, and Hans Kristian Eriksen. Lower growth rate from recent redshift space distortion measurements than expected from planck. *Physical review letters*, 111(16):161301, 2013.
- [48] Federico Marulli, Alfonso Veropalumbo, Lauro Moscardini, Andrea Cimatti, and Klaus Dolag. Redshift-space distortions of galaxies, clusters, and agn-testing how the accuracy of growth

rate measurements depends on scales and sample selections. *Astronomy & Astrophysics*, 599:A106, 2017.

- [49] Francisco-Shu Kitaura, Sergio Rodríguez-Torres, Chia-Hsun Chuang, Cheng Zhao, Francisco Prada, Hector Gil-Marín, Hong Guo, Gustavo Yepes, Anatoly Klypin, Claudia G Scóccola, et al. The clustering of galaxies in the sdss-iii baryon oscillation spectroscopic survey: mock galaxy catalogues for the boss final data release. *Monthly Notices of the Royal Astronomical Society*, 456(4):4156–4173, 2016.
- [50] Sergio A Rodríguez-Torres, Chia-Hsun Chuang, Francisco Prada, Hong Guo, Anatoly Klypin, Peter Behroozi, Chang Hoon Hahn, Johan Comparat, Gustavo Yepes, Antonio D Montero-Dorta, et al. The clustering of galaxies in the sdss-iii baryon oscillation spectroscopic survey: modelling the clustering and halo occupation distribution of boss cmass galaxies in the final data release. *Monthly Notices of the Royal Astronomical Society*, 460(2):1173–1187, 2016.
- [51] Cheng Zhao, Chia-Hsun Chuang, Julian Bautista, Arnaud de Mattia, Anand Raichoor, Ashley J Ross, Jiamin Hou, Richard Neveux, Charling Tao, Etienne Burtin, et al. The completed sdss-iv extended baryon oscillation spectroscopic survey: 1000 multi-tracer mock catalogues with redshift evolution and systematics for galaxies and quasars of the final data release. *Monthly Notices of the Royal Astronomical Society*, 503(1):1149–1173, 2021.
- [52] Kyle S Dawson, David J Schlegel, Christopher P Ahn, Scott F Anderson, Éric Aubourg, Stephen Bailey, Robert H Barkhouser, Julian E Bautista, Alessandra Beifiori, Andreas A Berlind, et al. The baryon oscillation spectroscopic survey of sdss-iii. *The Astronomical Journal*, 145(1):10, 2012.
- [53] Shadab Alam, Franco D Albareti, Carlos Allende Prieto, Friedrich Anders, Scott F Anderson, Timothy Anderton, Brett H Andrews, Eric Armengaud, Éric Aubourg, Stephen Bailey, et al. The eleventh and twelfth data releases of the sloan digital sky survey: final data from sdss-iii. *The Astrophysical Journal Supplement Series*, 219(1):12, 2015.
- [54] Daniel J Eisenstein, David H Weinberg, Eric Agol, Hiroaki Aihara, Carlos Allende Prieto, Scott F Anderson, James A Arns, Éric Aubourg, Stephen Bailey, Eduardo Balbinot, et al. Sdss-iii: Massive spectroscopic surveys of the distant universe, the milky way, and extra-solar planetary systems. *The Astronomical Journal*, 142(3):72, 2011.
- [55] Kyle S Dawson, Jean-Paul Kneib, Will J Percival, Shadab Alam, Franco D Albareti, Scott F Anderson, Eric Armengaud, Éric Aubourg, Stephen Bailey, Julian E Bautista, et al. The sdss-iv extended baryon oscillation spectroscopic survey: overview and early data. *The Astronomical Journal*, 151(2):44, 2016.
- [56] D Alonso, A Bueno Belloso, FJ Sánchez, J García-Bellido, and E Sánchez. Measuring the transition to homogeneity with photometric redshift surveys. *Monthly Notices of the Royal Astronomical Society*, 440(1):10–23, 2014.
- [57] R. S. Gonçalves, G. C. Carvalho, C. A. P. Bengaly, J. C. Carvalho, and J. S. Alcaniz. Measuring the scale of cosmic homogeneity with SDSS-IV DR14 quasars. *Mon. Not. Roy. Astron. Soc.*, 481(4):5270–5274, 2018.
- [58] Rodrigo S. Gonçalves, Gabriela C. Carvalho, Uendert Andrade, Carlos A. P. Bengaly, Joel C. Carvalho, and Jailson Alcaniz. Measuring the cosmic homogeneity scale with SDSS-IV DR16 Quasars. *JCAP*, 03:029, 2021.
- [59] D. Alonso, A. Bueno belloso, F. J. Sánchez, J. García-Bellido, and E. Sánchez. Measuring the transition to homogeneity with photometric redshift surveys. *Mon. Not. Roy. Astron. Soc.*, 440(1):10–23, 2014.
- [60] Uendert Andrade, Rodrigo S. Gonçalves, Gabriela C. Carvalho, Carlos A. P. Bengaly, Joel C. Carvalho, and Jailson Alcaniz. The angular scale of homogeneity with SDSS-IV DR16 luminous red galaxies. *JCAP*, 10:088, 2022.

- [61] Beth Reid, Shirley Ho, Nikhil Padmanabhan, Will J Percival, Jeremy Tinker, Rita Tojeiro, Martin White, Daniel J Eisenstein, Claudia Maraston, Ashley J Ross, et al. Sdss-iii baryon oscillation spectroscopic survey data release 12: galaxy target selection and large-scale structure catalogues. *Monthly Notices of the Royal Astronomical Society*, 455(2):1553–1573, 2016.
- [62] Pierros Ntelis et al. Exploring cosmic homogeneity with the BOSS DR12 galaxy sample. *JCAP*, 06:019, 2017.
- [63] Ashley J Ross, Julian Bautista, Rita Tojeiro, Shadab Alam, Stephen Bailey, Etienne Burtin, Johan Comparat, Kyle S Dawson, Arnaud De Mattia, Héliion du Mas des Bourboux, et al. The completed sdss-iv extended baryon oscillation spectroscopic survey: Large-scale structure catalogues for cosmological analysis. *Monthly Notices of the Royal Astronomical Society*, 498(2):2354–2371, 2020.
- [64] Julian E Bautista, Romain Paviot, Mariana Vargas Magaña, Sylvain de La Torre, Sebastien Fromenteau, Hector Gil-Marín, Ashley J Ross, Etienne Burtin, Kyle S Dawson, Jiamin Hou, et al. The completed sdss-iv extended baryon oscillation spectroscopic survey: measurement of the bao and growth rate of structure of the luminous red galaxy sample from the anisotropic correlation function between redshifts 0.6 and 1. *Monthly Notices of the Royal Astronomical Society*, 500(1):736–762, 2021.
- [65] Seshadri Nadathur, Alex Woodfinden, Will J Percival, Marie Aubert, Julian Bautista, Kyle Dawson, Stéphanie Escoffier, Sebastien Fromenteau, Héctor Gil-Marín, James Rich, et al. The completed sdss-iv extended baryon oscillation spectroscopic survey: geometry and growth from the anisotropic void–galaxy correlation function in the luminous red galaxy sample. *Monthly Notices of the Royal Astronomical Society*, 499(3):4140–4157, 2020.
- [66] Hume A Feldman, Nick Kaiser, and John A Peacock. Power spectrum analysis of three-dimensional redshift surveys. *arXiv preprint astro-ph/9304022*, 1993.
- [67] Prakash Sarkar, Jaswant Yadav, Biswajit Pandey, and Somnath Bharadwaj. The scale of homogeneity of the galaxy distribution in SDSS DR6. *Mon. Not. Roy. Astron. Soc.*, 399:L128–L131, 2009.
- [68] Morag Scrimgeour et al. The WiggleZ Dark Energy Survey: the transition to large-scale cosmic homogeneity. *Mon. Not. Roy. Astron. Soc.*, 425:116–134, 2012.
- [69] Biswajit Pandey. A method for testing the cosmic homogeneity with Shannon entropy. *Mon. Not. Roy. Astron. Soc.*, 430:3376, 2013.
- [70] Biswajit Pandey and Suman Sarkar. Testing homogeneity in the Sloan Digital Sky Survey Data Release Twelve with Shannon entropy. *Mon. Not. Roy. Astron. Soc.*, 454(3):2647–2656, 2015.
- [71] Suman Sarkar and Biswajit Pandey. An information theory based search for homogeneity on the largest accessible scale. *Mon. Not. Roy. Astron. Soc.*, 463(1):L12–L16, 2016.
- [72] Pierre Laurent et al. A  $14 h^{-3} \text{ Gpc}^3$  study of cosmic homogeneity using BOSS DR12 quasar sample. *JCAP*, 11:060, 2016.
- [73] Yigon Kim, Chan-Gyung Park, Hyerim Noh, and Jai-chan Hwang. CMASS galaxy sample and the ontological status of the cosmological principle. *Astron. Astrophys.*, 660:A139, 2022.
- [74] Francesco Sylos Labini, Nikolay L. Vasilyev, Yuriy V. Baryshev, and Martin Lopez-Corredoira. Absence of anti-correlations and of baryon acoustic oscillations in the galaxy correlation function from the Sloan Digital Sky Survey DR7. *Astron. Astrophys.*, 505:981–990, 2009.
- [75] Francesco Sylos Labini. Very large scale correlations in the galaxy distribution. *EPL*, 96(5):59001, 2011.

- [76] Chan-Gyung Park, Hwasu Hyun, Hyerim Noh, and Jai-chan Hwang. The cosmological principle is not in the sky. *Mon. Not. Roy. Astron. Soc.*, 469(2):1924–1931, 2017.
- [77] Asta Heinesen. Cosmological homogeneity scale estimates are dressed. *JCAP*, 10:052, 2020.
- [78] David Alonso, Ana Isabel Salvador, Francisco Javier Sánchez, Maciej Bilicki, Juan García-Bellido, and Eusebio Sánchez. Homogeneity and isotropy in the Two Micron All Sky Survey Photometric Redshift catalogue. *Mon. Not. Roy. Astron. Soc.*, 449(1):670–684, 2015.
- [79] R. S. Gonçalves, G. C. Carvalho, C. A. P. Bengaly, J. C. Carvalho, A. Bernui, J. S. Alcaniz, and R. Maartens. Cosmic homogeneity: a spectroscopic and model-independent measurement. *Mon. Not. Roy. Astron. Soc.*, 475(1):L20–L24, 2018.
- [80] Pierros Ntelis, Anne Ealet, Stephanie Escoffier, Jean-Christophe Hamilton, Adam James Hawken, Jean-Marc Le Goff, James Rich, and Andre Tilquin. The scale of cosmic homogeneity as a standard ruler. *JCAP*, 12:014, 2018.
- [81] Pierros Ntelis, Adam James Hawken, Stephanie Escoffier, Anne Ealet, and Andre Tilquin. Cosmological constraints from cosmic homogeneity. 4 2019.
- [82] Savvas Nesseris and Manuel Trashorras. Can the homogeneity scale be used as a standard ruler? *Phys. Rev. D*, 99(6):063539, 2019.
- [83] Martín Crocce, Anna Cabré, and Enrique Gaztanaga. Modelling the angular correlation function and its full covariance in photometric galaxy surveys. *Monthly Notices of the Royal Astronomical Society*, 414(1):329–349, 2011.
- [84] Stephen D Landy and Alexander S Szalay. Bias and variance of angular correlation functions. *Astrophysical Journal, Part 1 (ISSN 0004-637X)*, vol. 412, no. 1, p. 64–71., 412:64–71, 1993.
- [85] Micael Jarvis, Gary Bernstein, and Bhuvnesh Jain. The skewness of the aperture mass statistic. *Monthly Notices of the Royal Astronomical Society*, 352(1):338–352, 2004.
- [86] Antony Lewis, Anthony Challinor, and Anthony Lasenby. Efficient computation of cosmic microwave background anisotropies in closed friedmann-robertson-walker models. *The Astrophysical Journal*, 538(2):473, 2000.
- [87] R. E. Smith, J. A. Peacock, A. Jenkins, S. D. M. White, C. S. Frenk, F. R. Pearce, P. A. Thomas, G. Efstathiou, and H. M. P. Couchman. Stable clustering, the halo model and non-linear cosmological power spectra. *Monthly Notices of the Royal Astronomical Society*, 341(4):1311–1332, June 2003.
- [88] Eric V. Linder and Robert N. Cahn. Parameterized Beyond-Einstein Growth. *Astropart. Phys.*, 28:481–488, 2007.
- [89] Román Scoccimarro. Redshift-space distortions, pairwise velocities, and nonlinearities. *Physical Review D—Particles, Fields, Gravitation, and Cosmology*, 70(8):083007, 2004.
- [90] Atsushi Taruya, Takahiro Nishimichi, and Shun Saito. Baryon acoustic oscillations in 2d: Modeling redshift-space power spectrum from perturbation theory. *Physical Review D—Particles, Fields, Gravitation, and Cosmology*, 82(6):063522, 2010.
- [91] Uroš Seljak and Patrick McDonald. Distribution function approach to redshift space distortions. *Journal of Cosmology and Astroparticle Physics*, 2011(11):039, 2011.
- [92] Yi Wang, Pierre-Marc Jodoin, Fatih Porikli, Janusz Konrad, Yannick Benezeth, and Prakash Ishwar. C3net 2014: An expanded change detection benchmark dataset. In *Proceedings of the IEEE conference on computer vision and pattern recognition workshops*, pages 387–394, 2014.
- [93] Daniel Thomas, Oliver Steele, Claudia Maraston, J Johansson, Alessandra Beifiori, Janine Pforr, G Strömbäck, CA Tremonti, D Wake, D Bizyaev, et al. Stellar velocity dispersions and emission line properties of sdss-iii/boss galaxies. *Monthly Notices of the Royal Astronomical Society*, 431(2):1383–1397, 2013.

- [94] Faizan G Mohammad, Sylvain de la Torre, Davide Bianchi, Luigi Guzzo, and John A Peacock. Group–galaxy correlations in redshift space as a probe of the growth of structure. *Monthly Notices of the Royal Astronomical Society*, 458(2):1948–1963, 2016.
- [95] Martin White, M Blanton, A Bolton, D Schlegel, J Tinker, A Berlind, L Da Costa, E Kazin, Y-T Lin, M Maia, et al. The clustering of massive galaxies at  $z \approx 0.5$  from the first semester of boss data. *The Astrophysical Journal*, 728(2):126, 2011.
- [96] Sebastián E Nuza, Ariel G Sánchez, Francisco Prada, Anatoly Klypin, David J Schlegel, Stefan Gottlöber, Antonio D Montero-Dorta, Marc Manera, Cameron K McBride, Ashley J Ross, et al. The clustering of galaxies at  $z \simeq 0.5$  in the sdss-iii data release 9 boss-cmass sample: a test for the  $\lambda$  cdm cosmology. *Monthly Notices of the Royal Astronomical Society*, 432(1):743–760, 2013.
- [97] Shirley Ho, Antonio Cuesta, Hee-Jong Seo, Roland De Putter, Ashley J Ross, Martin White, Nikhil Padmanabhan, Shun Saito, David J Schlegel, Eddie Schlafly, et al. Clustering of sloan digital sky survey iii photometric luminous galaxies: The measurement, systematics, and cosmological implications. *The Astrophysical Journal*, 761(1):14, 2012.
- [98] Johan Comparat, Eric Jullo, Jean-Paul Kneib, Carlo Schimd, HuanYuan Shan, Thomas Erben, Olivier Ilbert, Joel Brownstein, Anne Ealet, Stephanie Escoffier, et al. Stochastic bias of colour-selected bao tracers by joint clustering–weak lensing analysis. *Monthly Notices of the Royal Astronomical Society*, 433(2):1146–1160, 2013.
- [99] Gil-Marín Héctor, Noreña Jorge, Verde Licia, Wagner Christian, Manera Marc, et al. The power spectrum and bispectrum of sdss dr11 boss galaxies–i. bias and gravity. *Mon. Not. Roy. Astron. Soc.*, 451:539–580, 2015.
- [100] S Basilakos, M Plionis, and C Ragone-Figueroa. The halo mass-bias redshift evolution in the  $\lambda$ cdm cosmology. *The Astrophysical Journal*, 678(2):627, 2008.
- [101] Pierros Ntelis, Anne Ealet, Stephanie Escoffier, Jean-Christophe Hamilton, Adam James Hawken, Jean-Marc Le Goff, James Rich, and Andre Tilquin. The scale of cosmic homogeneity as a standard ruler. *Journal of Cosmology and Astroparticle Physics*, 2018(12):014, 2018.
- [102] RFL Holanda, RS Gonçalves, JE Gonzalez, and JS Alcaniz. An estimate of the dark matter density from galaxy clusters and supernovae data. *Journal of Cosmology and Astroparticle Physics*, 2019(11):032, 2019.
- [103] A Semenaite, AG Sánchez, A Pezzotta, J Hou, R Scoccimarro, A Eggemeier, M Crocce, CH Chuang, A Smith, C Zhao, et al. Cosmological implications of the full shape of anisotropic clustering measurements in boss and eboss, arxiv e-prints (nov., 2021). *arXiv preprint arXiv:2111.03156*, 2111.
- [104] Ashley J Ross, Lado Samushia, Cullan Howlett, Will J Percival, Angela Burden, and Marc Manera. The clustering of the sdss dr7 main galaxy sample–i. a 4 per cent distance measure at  $z = 0.15$ . *Monthly Notices of the Royal Astronomical Society*, 449(1):835–847, 2015.
- [105] Shadab Alam, Metin Ata, Stephen Bailey, Florian Beutler, Dmitry Bizyaev, Jonathan A Blazek, Adam S Bolton, Joel R Brownstein, Angela Burden, Chia-Hsun Chuang, et al. The clustering of galaxies in the completed sdss-iii baryon oscillation spectroscopic survey: cosmological analysis of the dr12 galaxy sample. *Monthly Notices of the Royal Astronomical Society*, 470(3):2617–2652, 2017.
- [106] Shadab Alam, Marie Aubert, Santiago Avila, Christophe Balland, Julian E Bautista, Matthew A Bershad, Dmitry Bizyaev, Michael R Blanton, Adam S Bolton, Jo Bovy, et al. Completed sdss-iv extended baryon oscillation spectroscopic survey: Cosmological implications from two decades of spectroscopic surveys at the apache point observatory. *Physical Review D*, 103(8):083533, 2021.